Research article **Geoenergy**

https://doi.org/10.1144/geoenergy2025-024 | Vol. 4 | 2026 | geoenergy2025-024

Regional geomechanical response to large-scale CO_2 storage in the Bunter Sandstone Formation, UK Southern North Sea

John D. O. Williams[1*], Gareth A. Williams[2], Mark W. Fellgett[1], Lucy Abel[1] and Paul Bridger[1]

[1] British Geological Survey, Nicker Hill, Keyworth, Nottingham NG12 5GG, UK
[2] British Geological Survey, Cardiff University, Room 0.73 Main Building, Park Place, Cardiff CF10 3AT, UK
JDOW, 0000-0003-0177-9848; MWF, 0000-0001-7969-0021
* Correspondence: jdow@bgs.ac.uk

Abstract: The Bunter Sandstone Formation is the intended storage formation for several commercial CO_2 storage projects in the UK Southern North Sea. Previous studies have highlighted the potential for regional pressure perturbations expected to impact an area far beyond the storage sites where CO_2 will be contained by structural trapping. This study evaluates the potential geomechanical impacts associated with widespread pressurization of saline aquifers, based on a coupled flow–geomechanical modelling study. A published industrial-scale scenario is used as the basis for a reservoir simulation study, which envisages storage of 232 Mt, divided between four sites over a period of 30 years. Several scenarios are considered, with the worst-case scenario resulting in the greatest pressure increases selected for input into a geomechanical model. The results indicate that the saline aquifer is expected to experience only very small strains and gentle uplift of the seabed as a consequence of the modelled injection loads, with minimal risk to containment or other adverse impacts associated with rock failure. The large, well-connected nature of the saline aquifer ameliorates the potentially negative impacts of excessive pressurization. The modelling results suggest that the Bunter Sandstone Formation is an excellent prospect for commercial-scale storage of CO_2 from a geomechanical perspective.

Thematic collection: This article is part of the characterization and monitoring of containment in subsurface CO_2 storage collection available at: https://www.lyellcollection.org/topic/collections/containment

Received 10 June 2025; **revised** 29 April 2026; **accepted** 31 July 2026

Large-scale CO_2 storage in saline aquifers will be required to achieve globally significant reductions in greenhouse gas emissions through carbon capture and storage (CCS) (Ringrose *et al.* 2021). This is likely to involve developing multiple sites to optimize the storage capacity of such formations. The Bunter Sandstone Formation of the UK Southern North Sea (UK SNS) stands as an exemplar of an extensive saline aquifer licensed for storage of CO_2 at multiple sites. The North Sea Transition Authority (NSTA), the UK licensing authority for carbon storage, have granted licences for several large anticlinal traps in the northern part of the UK SNS (Gluyas and Bagudu 2020; Hollinsworth *et al.* 2022, 2024). The region of principal interest corresponds to the Silverpit Basin, a sub-basin of the UK SNS (Fig. 1). While gas has been produced from a limited number of Bunter Sandstone Formation structures in this region (Williams *et al.* 2014), most of the storage licences target saline aquifer storage prospects rather than depleted gas fields. This paper presents a numerical flow and geomechanical modelling study to evaluate the regional geomechanical impacts of a proposed multi-site CO_2 storage scheme.

The Bunter Sandstone Formation saline aquifer in the Silverpit Basin is bounded by a series of major faults and salt structures (Fig. 1). To date, seismic interpretation within the basin has not identified any laterally extensive internal fault systems with substantive offset that might form long-term barriers to flow in the Bunter Sandstone Formation, with most faults restricted to local structures (Hollinsworth *et al.* 2022; Abel *et al.* 2025; De Luca *et al.* 2025). Pore pressure measurements also indicate that the region is subject to a pressure regime distinct from adjacent sub-basins (Abel *et al.* 2025; Williams 2025). This implies that the Bunter Sandstone Formation of the Silverpit Basin can be approximated by a closed compartment at internal pressure equilibrium prior to CO_2 injection (Abel *et al.* 2025). Modelling of pressure depletion and recovery data from the Esmond gas field supports this view, indicating good aquifer connectivity within the Silverpit Basin over the gas production life cycle (Bentham *et al.* 2017).

The possibility of localized subseismic-scale temporary flow barriers remains, however. Indeed, faults in the overburden above the reservoir have been observed (BP 2021*c*), and operators have developed a multi-well injection strategy based on their location to mitigate the potential for on-structure compartmentalization (BP 2021*c*).

Several previous studies have investigated the potential pressure response to injection in the Silverpit Basin region, suggesting that large-scale injection of CO_2 would result in elevated pore pressures across the region (Smith *et al.* 2011; Noy *et al.* 2012; Agada *et al.* 2017; De Luca *et al.* 2025). These studies demonstrate that while the CO_2 is expected to be contained within the intended structural traps, the pressure response would be felt far more widely. The studies also invoke the role of a seabed subcrop of the Bunter Sandstone Formation in allowing pressure relief through the displacement of brine to the water column. This subcrop occurs above a high-relief salt dome where the Bunter Sandstone Formation has been uplifted to the surface (location shown in Fig. 1). While uncertainty exists relating to the connectivity between the subcrop and the proposed injection sites, no significant barriers to flow have been identified to date. The extent to which the subcrop will allow communication between the saline aquifer fluids and the seawater column is also uncertain (Noy *et al.* 2012).

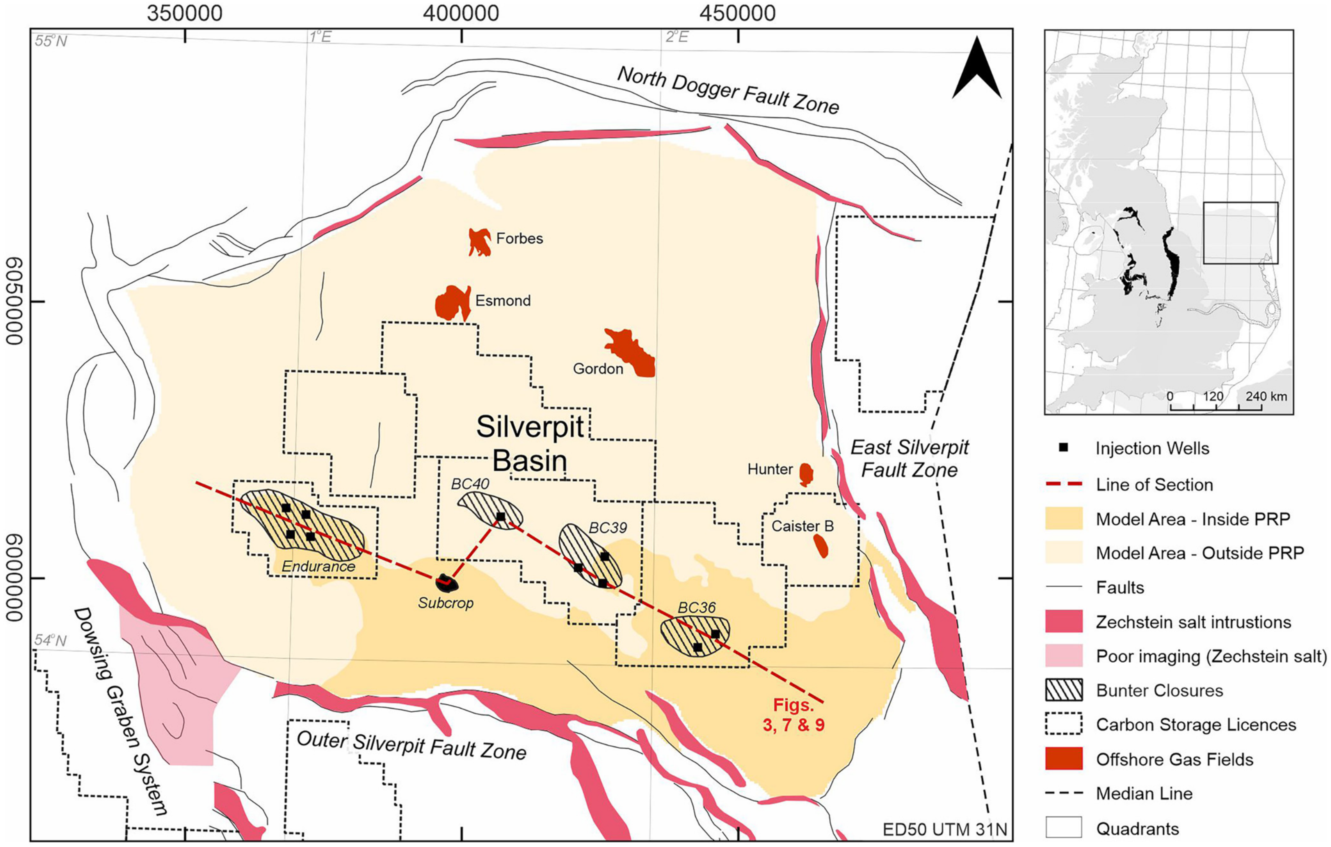

Fig. 1. Location map showing the model area within the Silverpit Basin. The model extent is shown by the yellow and orange shaded area broadly covering the Silverpit Basin, which is thought to represent a single connected aquifer unit forming an isolated pressure compartment at Bunter Sandstone Formation level. A seismic phase reversal polygon (PRP) appears to demarcate a zone of higher porosity and permeability (shaded dark orange) than the aquifer to the north (shaded yellow). The location of the main Bunter Closures (BC) targeted for CO_2 storage are indicated along with modelled injection wells. Source: the bounding structures shown are after Abel *et al.* (2025); the Bunter Sandstone Formation extent and outline are taken from Cameron *et al.* (1992) and the BC outlines are from CO_2Stored (Bentham *et al.* 2014); the offshore quadrant, carbon storage licence and gas field outlines, as well as the coastline linework, contains information provided by the North Sea Transition Authority and/or other third parties (https://opendata-nstauthority.hub.arcgis.com/search?collection=Dataset).

The issue of widely felt pressure increases in saline aquifers such as the Bunter Sandstone Formation has been identified as a potential challenge for multi-site CO_2 storage development (Bump and Hovorka 2024; Shoulders and Hodgkinson 2024). These challenges are commonly discussed in the context of pressure budgets, whereby pressure increases induced by one operation could potentially reduce the operational window available to adjacent projects. Bump and Hovorka (2023) also identified the risk of displacing formation fluids towards potentially transmissive features such as non-isolated wells and fracture systems, which may lead to contamination of freshwater or marine environments.

The potential for inducing widespread geomechanical responses is a further consideration that forms the focus of this study. Previous studies have evaluated the geomechanical response of individual Bunter Sandstone Formation structures for specific CO_2 storage development proposals (ETI 2016; National Grid 2016*a*; BP 2021*a*; Gibson-Poole *et al.* 2024). These site-specific models are generally concerned with whether the planned injection profiles can be achieved without locally damaging the top seal and posing a risk to CO_2 containment. However, in an extensive hydraulically connected saline aquifer formation, widespread changes to effective stress conditions could also lead to the following:

- induced seismicity;
- reservoir dilation leading to surface deformation; and
- cumulative stress–strain responses resulting from storage at multiple sites.

In addition to local effects, these processes could potentially occur at considerable distance from the storage sites themselves. While geomechanical effects remote from the storage site may not necessarily pose a CO_2 containment risk, they may have implications for induced seismicity or the displacement of other reservoir fluids such as highly saline or heavy metal enriched brine. Consequently, there may be a need to consider monitoring of pressure and/or strain more regionally beyond the storage sites. The relative importance of these risks will increase as further CO_2 storage developments seek to exploit the potential of saline aquifer formations, leading to an increase in the number of injection sites. Multi-site storage settings could potentially lead to amplification of risks otherwise considered minor in terms of likelihood and severity.

In this study, a regional geological model over the full extent of the Silverpit Basin area (Fig. 1) is used as the basis for a coupled flow and geomechanical modelling study to evaluate the impact of industrial-scale CO_2 injection at multiple sites. The modelled CO_2 injection schedule is taken from a commercial scenario published by a CO_2 storage licensee active in the region; the Northern Endurance Partnership (NEP) Path to 10 Mt Per Annum (Phase 2) Scenario (BP 2022). This scenario comprises injection into four different structural closures in the Silverpit Basin, with no pressure relief wells. The aim of the modelling is to determine what geomechanical impacts are likely to arise due to a credible multi-site storage scheme in a large hydraulically connected saline aquifer unit.

Geological setting

The study region forms part of the Southern Permian Basin, an east–west-striking depocentre extending across northern Europe from eastern England to Poland and the Baltic States (Doornenbal and Stevenson 2010). The stratigraphic and tectonic evolution of the basin is outlined in Figure 2, although detailed accounts of the geological evolution and exploration history are provided elsewhere (Cameron *et al.* 1992; Underhill 2003; Doornenbal and Stevenson 2010). The basin has received renewed interest in recent years due to its extensive energy transition opportunities (Doornenbal *et al.* 2022; Fyfe and Underhill 2023; Underhill *et al.* 2023). The Silverpit Basin forms a sub-basin within the UK SNS portion of the basin, which is bordered by the Dowsing Graben System to the west, the North Dogger Fault Zone to the north, the Cleaver Bank High to the east and the Outer Silverpit Fault Zone (Fig. 1). The combination of these major structural lineaments isolates the Silverpit Basin from the surrounding sub-basins (Abel *et al.* 2025). A further combination of faults and salt-wall structures, known as the East Silverpit Fault Zone, divides the main part of the Silverpit Basin from its eastern extension that extends into the Netherlands sector (Abel *et al.* 2025).

A thick cyclical sequence of carbonate–evaporite strata ascribed to the Permian-aged Zechstein Group (Fig. 2) exerted a key control on the subsequent structural evolution of the study region (Van Hoorn 1987; Allen *et al.* 1994; Griffiths *et al.* 1995; Stewart and Coward 1995; Brennan and Adam 2023; Brennan *et al.* 2023). The impact of the Zechstein Group on the current configuration of the study region is key to understanding the prospectivity of the Bunter Sandstone Formation for CO_2 storage (Fig. 3). After the Zechstein Sea receded at the end of the Permian, *c.* 400 m of distal floodplain and lacustrine mudstones of the Bunter Shale Formation were deposited during the Early Triassic. The Bunter Shale is overlain by the predominantly fluvial succession of the Bunter Sandstone Formation, the saline aquifer of principal interest for CO_2 storage in the Silverpit Basin. Both units are components of the Bacton Group (Fig. 2). Although the Bunter Sandstone Formation is 170 m thick on average, its thickness is variable across the study area, and it is progressively eroded beneath the Hardegsen Unconformity towards the north of the study area. The Hardegsen Unconformity separates the Bunter Sandstone Formation from the overlying top seals of the Haisborough Group (Geluk and Röhling 1997). The Haisborough Group predominantly comprises a sequence of red mudstones interbedded with dolomite and anhydrite beds. It also contains

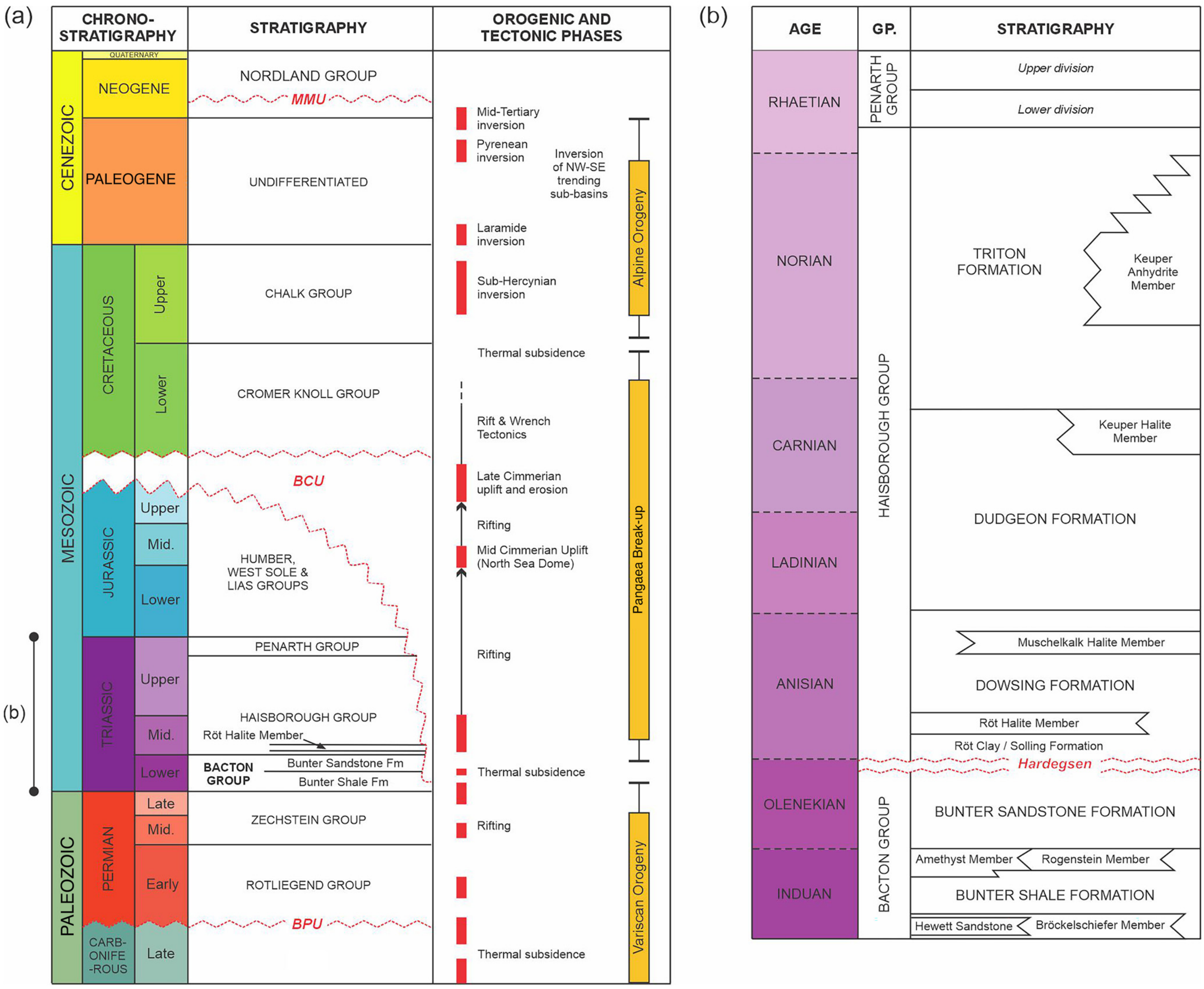

Fig. 2. (**a**) Tectonostratigraphic chart for the UK SNS. MMU: Mid Miocene Unconformity, BCU: Base Cretaceous Unconformity, BPU: Base Permian Unconformity. (**b**) Stratigraphic detail for the Triassic indicating the stratigraphic variation overlying the Bunter Sandstone Formation. Source: (a) adapted from Abel *et al.* (2025); the tectonic history was compiled from Glennie (1990), Doornenbal and Stevenson (2010) and Grant *et al.* (2019, 2020); (b) after Johnson *et al.* (1994).

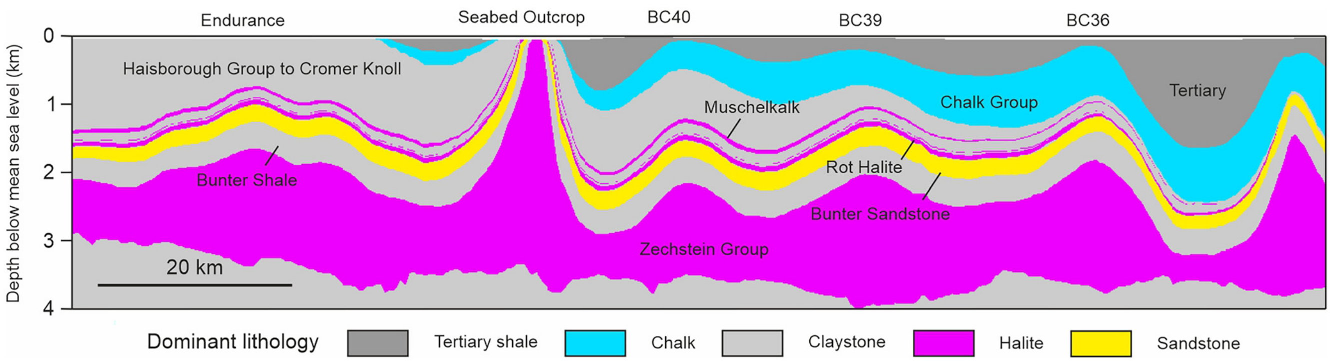

Fig. 3. Cross-section through the geological model indicating the main stratigraphic subdivisions and their dominant lithologies. The line of section is indicated in Figure 1.

several widespread halite members, the oldest of which, the Röt Halite Member, is present across almost the entire extent of the Silverpit Basin and forms a key component of the top seal for CO_2 storage (Cameron *et al.* 1992; Heinemann *et al.* 2012; Morris *et al.* 2026). An intervening claystone unit informally known as the Röt Clay separates the Bunter Sandstone Formation from the Röt Halite Member (Furnival *et al.* 2014; Gibson-Poole *et al.* 2024) and is laterally equivalent to the Solling Formation of the Netherlands sector.

The topography generated by salt mobilization influenced the lithology and thickness distributions of subsequent Jurassic strata, which were deposited in marine conditions when continued rifting combined with both regional thermal subsidence and eustatic sea-level rise (Van Hoorn 1987; Cameron *et al.* 1992; Stewart and Coward 1995; Doornenbal and Stevenson 2010). Cimmerian uplift and erosion commenced during the Upper Jurassic, leading to significant removal of Jurassic strata beneath the Base Cretaceous Unconformity (Fig. 2). Rifting and halokinesis continued into the Cretaceous when the Cromer Knoll and Chalk groups were deposited in marine environments. Further halokinesis during the Cenozoic continued to exert an important control on deposition (Underhill 2009). The resulting anticlinal domes and elongate structural accumulations form the dominant structural fabric of the Triassic and subsequent strata within the Silverpit Basin, with structural closures at the Bunter Sandstone Formation level forming the principal CO_2 storage play (Noy *et al.* 2012; Williams *et al.* 2013*a*, *b*, 2014; Hollinsworth *et al.* 2022).

The detailed sedimentology and diagenetic history of the Bunter Sandstone Formation in the Silverpit Basin are discussed in detail by Hossain *et al.* (2024) and Rushton *et al.* (2025). However, it is pertinent to note that seismic reflections from the top Bunter Sandstone Formation exhibit a distinct regionally extensive polarity reversal, which is observed across the south of the study area (Fig. 1). The resulting phase reversal polygon (PRP) is important due to observed differences in porosity in wells either side of the boundary (Furnival *et al.* 2014). This property variation is thought to result from pervasive halite cementation in the upper part of the Bunter Sandstone Formation to the north of the PRP (Blackbourn and Robertson 2014; Furnival *et al.* 2014).

Table 1. CO_2 injection schedule for the Northern Endurance Partnership (Phase 2) Path to 10 Mt Per Annum (BP 2022)

Date	Injection rate (Mt a^{-1})			
	Endurance	BC36	BC39	BC40
2026	4.00	0.00	0.00	0.00
2029	4.00	2.00	3.00	1.00
2051	0.00	0.00	0.00	0.00

BC refers to the Bunter Closure storage sites as defined in the UK's online storage atlas, CO_2Stored (Bentham *et al.* 2014).

Modelled CO_2 storage scenario

The CO_2 injection schedule modelled in this study was based on the Northern Endurance Partnership (Phase 2) Path to 10 Mt Per Annum (BP 2022). This scenario represents a projected expansion or build-out phase, following on from initial plans to store CO_2 at the Endurance storage site. A storage permit was granted for the Endurance site in 2024, with construction anticipated to commence in 2025. The scenario considers a total injected storage mass of 232 Mt, divided between four sites (Table 1): a nominal injection rate of 1 Mt a^{-1} per well has been used in the simulations.

Static reservoir model

Structural model

A geological model covering the extent of the connected aquifer volume within the Silverpit Basin (Fig. 1) was generated from regional seismic interpretation and well data catalogues available to the British Geological Survey. The available seismic database is described by Abel *et al.* (2025). Seven seismic horizons were interpreted on multiple 2D and 3D seismic surveys (see Abel *et al.* 2025 for more information) to allow depth conversion and geomechanical modelling of the overburden and underburden (Table 2). Two-way travel time data were gridded and depth-converted using the velocity model parameters shown in Table 2. The resulting depth surfaces were corrected to fit measured formation tops in available wells using a high surface tension, to avoid 'bull's eyes' located on individual well locations.

For geomechanical modelling purposes, the entire overburden succession to seabed, as well as the underlying surfaces, was integrated into the model, although only the sequence between the Zechstein Group and the Röt Halite Member (the Röt Clay, Bunter Sandstone and Bunter Shale formations) was activated in the dynamic flow simulations. Additional volumes were also appended to the sides and underburden of the geomechanical model grid to ensure that boundary stresses were equalized and to avoid grid buckling. A similar process to that described by Olden *et al.* (2012) was followed to construct the geomechanical model grid. These additional volumes were not activated in the dynamic flow simulations, which were truncated at the structural boundaries surrounding the western and central extent of the Silverpit Basin (Fig. 1). These structural boundaries are interpreted to form no-flow boundaries to the hydraulic unit (Smith *et al.* 2011; Noy *et al.* 2012; Abel *et al.* 2025).

A relatively coarse 400×400 m horizontal grid cell increment was used as a compromise between the need to incorporate

Table 2. Reference velocity V_0 and velocity gradient k parameters for the layer-cake velocity model used to depth convert the seismic travel-time surfaces

Top surface	Base surface	V_0 (m s^{-1})	k
0 m (MSL)	Seabed	1480	0.000
Seabed	Top Chalk Group	1788*	0.284*
Top Chalk Group	Base Cretaceous Unconformity	2256	0.860
Base Cretaceous Unconformity	Top Muschelkalk Halite Member	2735	0.239
Top Muschelkalk Halite Member	Top Bunter Sandstone Formation	3046	0.374
Top Bunter Sandstone Formation	Top Zechstein Formation	3269	0.316
Top Zechstein Formation	Top Rotliegend Group	4577	0.000

MSL, mean sea level.
*Velocity values for the Tertiary sequence were taken from Pluymaekers *et al.* (2017).

increased vertical resolution and the need to maintain reasonable simulation run times. The final model comprised 357 cells in the X (I) grid direction and 297 cells in the Y (J) direction. The cell size in the Z (K) direction was highly variable due to differences in lithostratigraphic unit thicknesses and their variation across the study region. Two grid versions were created with different vertical scales within the Bunter Sandstone Formation interval: in the fine-scale geological model, the Bunter Sandstone Formation interval was divided into thin layers *c*. 2.5 m in size to capture small-scale heterogeneities during petrophysical modelling. A coarse-scaled grid with an average cell size of 7.5 m in the reservoir interval was also generated so that the fine-scale model could be upscaled into a grid containing a tractable number of cells for simulation purposes.

Because seismically resolvable faults within the Silverpit Basin are highly localized, they are not expected to form significant regional barriers to fluid migration because the pressure front will eventually bypass the faulted section of reservoir. Subseismic-scale faults and deformation bands are frequently observed in Permo-Triassic outcrops onshore UK. Vosper *et al.* (2017) used an upscaling approach to investigate the impact of deformation bands in outcrop-scale fault zones on bulk formation permeability. The strongest impact on the permeability tensor occurred perpendicular to the deformation bands. Whilst subseismic-scale deformation could have a significant impact on near-well-bore injectivity, in the far-field formation fluids would be likely to be displaced along preferential flow paths non-orthogonal to the pressure front. It is envisaged this would result in a transient localized pressure increase around the deformation bands but would not significantly impact the propagation of the pressure front at a regional scale.

Consequently, a pragmatic decision was taken to exclude faults from the model. This carries the benefit of simplifying the mesh structure for the numerical modelling. However, a lack of faults is a limitation of the model, and so the potential presence of faults was considered during the analysis of the geomechanical modelling results discussed later.

Petrophysical model

Rock property measurements for the Bunter Sandstone Formation used to parameterize the reservoir model are summarized in Table 3. The data were compiled from an analysis of core plug measurements from 23 wells located within the study region (Noy *et al.* 2012; Furnival *et al.* 2014; Weatherford Laboratories 2015; National Grid 2016*a*). The data have been subdivided based on the well location relative to the interpreted PRP (Fig. 1). Core plug samples from within the PRP have higher porosity and permeability than samples from wells to the north of the PRP.

A model of the effective porosity distribution for the Bunter Sandstone Formation was computed by Gaussian random function simulation using a spherical variogram with an anisotropy range of 1200 m along the major/minor axis and 12 m in the Z direction. The horizontal permeability field was calculated from this porosity grid using a bivariate distribution, obtained from log-linear cross-plots of core plug porosity and horizontal permeability. The average modelled horizontal permeability value of 295 mD calculated for the Endurance storage site (Table 3) is slightly higher than the average formation permeability of 270 mD, as measured in a well test (National Grid 2016*b*). The mean modelled permeability of 55 mD outside the PRP is consistent with the bulk aquifer permeability estimated from a study that history matched the pressure recovery of a post-production well drilled in the Esmond gas field (Bentham *et al.* 2017). It falls between the geometric mean (42 mD) and median (72 mD) measured core plug permeability. These values are consistent with the petrophysical analysis carried

Table 3. Rock properties for the Bunter Sandstone Formation obtained from laboratory core plug measurements and petrophysical analysis

Property	Outside seismic PRP	Inside seismic PRP
Core plug porosity		
Minimum porosity (m^3 m^{-3})	0.01	0.04
Maximum porosity (m^3 m^{-3})	0.38	0.33
Arithmetic average porosity (m^3 m^{-3})	0.19	0.22
Standard deviation porosity (m^3 m^{-3})	0.07	0.05
Wireline log porosity		
Arithmetic average total porosity (m^3 m^{-3})	0.20	0.22
Arithmetic average effective porosity (m^3 m^{-3})	0.16	0.20
Core plug permeability		
Minimum K_H (mD)	0.01	0.06
Maximum K_H (mD)	8730.00	10 841.00
Arithmetic average K_H (mD)	397.93	737.90
Geometric average K_H (mD)	42.04	240.00
Harmonic average K_H (mD)	0.68	8.70
Standard deviation K_H (mD)	752.43	1211.10
K_V/K_H	$K_V \approx 0.6K_H$	$K_V \approx 0.6K_H$
Static reservoir model rock properties		
Minimum effective porosity (m^3 m^{-3})	0.005	0.02
Maximum effective porosity (m^3 m^{-3})	0.30	0.30
Average effective porosity (m^3 m^{-3})	0.153	0.20
Standard deviation effective porosity (m^3 m^{-3})	0.06	0.04
Minimum K_H (mD)	0.27	0.34
Maximum K_H (mD)	790.00	3188.00
Average K_H (mD)	55.00	295.00
Standard deviation K_H (mD)	87.00	348.00
Reservoir net/gross (NTG) ratio	0.85	0.95
Pore compressibility (bar^{-1})	5.6×10^{-5}	5.6×10^{-5}
Thermal conductivity (W m^{-1} °C^{-1})	4.50	4.50
Specific heat capacity (J kg^{-1} °C^{-1})	1045.00	1045.00
Density (kg m^{-3})	2660	2660

The final reservoir model porosity and permeability fields were calculated using Gaussian random function simulation. Thermal properties were taken from Hartmann and Pechnig (2008) and Kleiner (2003).

out by the current operators of the Endurance site (Gibson-Poole *et al.* 2024), who derived average permeabilities of 298 mD inside the Endurance storage site and 54 mD for the surrounding aquifer.

The ratio (K_V/K_H) of vertical (K_V) to horizontal (K_H) permeability from core plug measurements is *c*. 0.6. However, well-test data obtained by National Grid Carbon (Furnival *et al.* 2014; National Grid 2016*a*) measured a K_V/K_H ratio of between 0.10 and 0.36 with a vertical interference test and 0.04 using a drill stem test (DST). In this study we use a base-case value for K_V/K_H of 0.1, with an upper bound of 0.36 and a lower bound of 0.01, closer to the DST.

A constant net/gross (NTG) ratio of 0.95 has been used in the reservoir model to represent the Bunter Sandstone Formation interval inside the seismic PRP. This is comparable with the average NTG calculated by Gibson-Poole *et al.* (2024) for the reservoir interval at the Endurance site. A lower NTG of 0.85 has been applied to the model outside this region, higher than the average value of 0.7 calculated for the more localized region around Endurance by Gibson-Poole *et al.* (2024).

The modelled top seal comprises an interbedded mudstone–salt sequence, and the reservoir is underlain by a thick layer of predominantly siltstone and mudstone (the Bunter Shale Formation). Halite rock properties were taken from measurements made on Messinian salt rocks by Samperi *et al.* (2020) (Table 4). Mudstone layers in the model were assigned a constant average porosity and permeability (Table 4), based on measurements taken from samples of the Mercia Mudstone Group (MMG) sediments onshore UK (Jin *et al.* 2010; Armitage *et al.* 2016; Harrington *et al.* 2018). The MMG forms the onshore lateral equivalent to the Haisborough Group in the UK SNS. Permeabilities ranged from 2.1×10^{-3} to 8.5×10^{-6} mD, with an arithmetic mean of 1.4×10^{-3} mD and a geometric mean of 3.6×10^{-4} mD. Sample porosities ranged between 0.05 and 0.22 porosity fraction. A porosity of 0.1, a K_H of 5.0×10^{-3} mD and a K_V/K_H ratio of 0.1 were used for the shale horizons, consistent with Jin *et al.* (2010).

Multiphase fluid properties

Two sets of Bunter Sandstone Formation relative permeability curves were used in this study, corresponding to the base case and downside model scenarios published in key knowledge documents from the NEP (BP 2021*b*). These follow a modified Corey power-law model (Corey 1954; Brooks and Corey 1964) with the parameters shown in Table 5. The Bunter Sandstone Formation capillary pressure curve is based on a Skjaeveland *et al.* (2000) model fit to laboratory measurements on core from the Endurance site (National Grid 2016*b*). A single set of relative permeability and capillary pressure curves was used to represent the top seal and underburden sequence (Table 5). The curves were based on a modified Corey power-law fitted to measurements from the Calmar Shale (Bennion and Bachu 2006).

The range in pore compressibility represents a significant source of uncertainty. Pore compressibility measurements on Bunter Sandstone Formation samples gave a range between 1.65×10^{-5} and 4.5×10^{-5} bar^{-1} (Jin *et al.* 2010). A compilation of pore compressibility measurements from oil and gas fields on the UK Continental Shelf (UKCS) (Jin *et al.* 2010) gave a range between 4.0×10^{-5} and 15.0×10^{-5} bar^{-1}, with a mean of 5.0×10^{-5} bar^{-1}, close to the value of 5.6×10^{-5} bar^{-1} predicted by the relationship of Hall (1953) for a reservoir porosity of 0.18. Wiese *et al.* (2010) used a value of 7.2×10^{-5} bar^{-1} in their simulations of CO_2 injection at the Ketzin pilot site. Lower and upper bound values of 2.5×10^{-5} and 8.5×10^{-5} bar^{-1} are calculated based on correlations published by Horne (1990) and Jalalh (2006*a*, *b*), respectively. As the measured values show considerable spread, a pore compressibility of 5.6×10^{-5} bar^{-1} is considered reasonable and is used here.

Mudstone layers representing the Röt Clay top seal and the Bunter Shale Formation underburden sequence have also been included in the model. These were assigned a pore compressibility of 5.6×10^{-4} bar^{-1}, comparable in magnitude to measurements made on MMG samples by Jin *et al.* (2010) and Harrington *et al.* (2018), who recorded a range of pore compressibility values between 2.6×10^{-5} and 1.0×10^{-4} bar^{-1}.

Halite layers were also included in thermal model runs to capture the geomechanical effects of a low-temperature plume developed in response to cold CO_2 injection on halite stability. These layers were assigned a pore compressibility of 5.6×10^{-18} bar^{-1}. Robertson *et al.* (1958) measured an average halite compressibility of 4.17×10^{-18} bar^{-1} in a series of laboratory experiments.

The thermal conductivity and specific heat capacity assigned to each modelled rock type are summarized in Tables 3 and 4. Salt thermal properties were taken from Robertson *et al.* (1958), Samperi *et al.* (2020) and Raymond *et al.* (2022). Shale thermal properties were based on a series of measurements made on samples of MMG by Parkes *et al.* (2021). Bunter Sandstone Formation thermal properties were taken from Kleiner (2003) and Hartmann and Pechnig (2008).

Dynamic reservoir model

A series of flow simulations were conducted to test the effects of key model uncertainties on the amount of CO_2 stored and the resulting pressure field (Table 6). The scenarios were designed to progressively limit the CO_2 storage capacity of the aquifer by varying model parameters within realistic bounds. The total injected mass of CO_2 achieved in each simulation, together with the maximum percentage of the fracture pressure reached in the reservoir, are summarized in Table 7.

Multiphase fluid flow modelling was undertaken using the PFLOTRAN-OGS open-source reservoir simulator package (Hammond 2016; OpenGoSim 2021). PFLOTRAN-OGS has a

Table 4. Overburden and underburden rock properties used in the models

Property	Salt	Mudstone
Porosity (m^3 m^{-3})	1.0×10^{-6}	0.10
K_H (mD)	5.0×10^{-5}	0.005
K_V (mD)	5.0×10^{-6}	0.0005
Pore compressibility (bar^{-1})	5.6×10^{-18}	5.6×10^{-4}
Thermal conductivity (W m^{-1} °C^{-1})	5.40	2.50
Specific heat capacity (J kg^{-1} °C^{-1})	1200.00	913.00
Density (kg m^{-3})	2160.00	2456.00

Salt-rock porosity measurements were taken from Samperi *et al.* (2020). Mudstone values are based on measurements made on samples of the Mercia Mudstone Group (Armitage *et al.* 2016) and Solling Claystone (Spain and Conrad 1997). Salt thermal properties were taken from Robertson *et al.* (1958), Samperi *et al.* (2020) and Raymond *et al.* (2022). Shale thermal properties were taken from a series of measurements made on samples of Mercia Mudstone Group rocks by Parkes *et al.* (2021).

Table 5. Modified Corey model parameters for the relative permeability curves used in the simulations

	NEP downside	NEP base case	Calmar Shale
S_{birr}	0.25	0.20	0.26
$S_{c\,CO_2}$	0.40	0.35	0.64
m	6.00	4.00	2.47
n	3.50	2.50	1.30
$k_{rmax}CO_2$	0.70	0.70	0.18

NEP scenarios after BP (2021*b*). S_{birr}, irreducible bulk gas saturation; S_{cCO_2}, critical CO_2 saturation; m and n, Corey exponents; $k_{rmax}CO_2$, Relative permeability endpoint CO_2.

Table 6. Sensitivity analysis to test the effects of key simulation uncertainties on the amount of stored CO_2 and the pressure field

Simulation scenario run	Description
1	Base case
2	Test effect of shutting the seabed outcrop
3	Test effect of impermeable top and base boundary conditions
4	Test effect of impermeable top and base boundary conditions, and shutting the seabed outcrop
5	Test effect of reducing K_V/K_H to 0.01 (0.04 DST) – base case is 0.1
6	Test effect of increasing K_V/K_H to 0.36 (maximum from VIT and core plug data) – base case is 0.1
7	$K_H = 0.65K_H$ base case (to match lower-bound permeability from the Esmond pressure recovery model, see Bentham *et al.* 2017); K_V/K_H 0.1
8	$K_H = 0.65K_H$ base case; $K_V/K_H = 0.01$
9	$K_H = 0.65K_H$ base case; K_V/K_H 0.01; NEP downside relative permeability curves
10	$K_H = 0.65K_H$ base case; K_V/K_H 0.01; NEP downside relative permeability curves; seabed outcrop shut off from reservoir
11	As Scenario 10, with bottomhole pressure (BHP) set to allow the full amount of CO_2 to be injected at each well location

Note that the CO_2 injection rate is controlled by the BHP in simulations 1–10, with the pressure threshold set to the Bunter Sandstone Formation fracture closure pressure at the top of the well perforations.
DST, drill stem test; VIT, vertical interference test; K_H, horizontal permeability; K_V, vertical permeability.

built-in two-phase (gas and water) model specifically adapted for CO_2 storage. This model allows the aqueous phase to contain dissolved gas, and the gas phase to contain vaporized water. The thermo-physical properties of the CO_2 phase are computed internally within the simulator, using the equation of state developed by Span and Wagner (1996). The density, viscosity, internal energy and enthalpy of pure water are taken from the International Formulation Committee (IFC) steam tables (IFC 2010). The water density and viscosity are then corrected to account for salinity using the correlations of Batzl and Wang (1992), whilst the density correction necessary to account for a dissolved CO_2 component uses the formulation proposed by Duan *et al.* (2008). The amount of CO_2 dissolved in the formation brine is calculated using empirical formulations developed by Duan and Sun (2003).

All regional models were run in isothermal mode. The temperature gradient established during equilibration was used to calculate brine and gas fluid properties, and initial cell temperatures were maintained throughout the simulation run. To evaluate the role of thermal effects, a local simulation of CO_2 injection into the Endurance structure was also run using a refined grid in thermal mode. In this case, the simulator solves for energy conservation, and fluid properties are updated according to evolving cell temperatures.

The models were initialized using a hydrostatic pressure gradient of 10.94 kPa m^{-1}, a seabed temperature of 10.75°C and a geothermal gradient of 34°C km^{-1}. A linear salinity gradient (equation 1) has been derived from measurements made at the Endurance site, and wells in the Forbes, Esmond and Caister B gas fields were used to establish hydrostatic equilibrium.

$$\mathrm{TDS} = 135.0Z + 52589 \qquad (1)$$

where TDS are the total dissolved solids (mg kg^{-1}) and Z is vertical depth below seabed (m).

The geological model is thought to cover a single isolated pressure compartment (Abel *et al.* 2025), so all boundaries of the computational grid were assigned a no-flow condition. A series of flux boundary conditions have been assigned to cells penetrated by injection wells to achieve the target CO_2 injection rates in Table 1. Fracture pressures calculated at the well perforations were used to set bottomhole pressure (BHP) constraints on the CO_2 injection rate in scenarios 1–10 (Table 6). A fracture pressure gradient of 16.8 MPa km^{-1} was assumed based on fracture closure pressures estimated from minifrac data for the Bunter Sandstone Formation at the Endurance site (BP 2021*a*). In Scenario 11, the BHP constraint was set to a nominal high value (60 MPa) to allow the full amount of CO_2 to be injected at each well location (effectively disabling the BHP constraint). In this case, a maximum pressure of 47.4 MPa (an overpressure of 11.5 MPa) occurred in the cells containing the injection wells in Bunter Closure 39 (Fig. 1), where reservoir permeability is reduced relative to the rest of the model.

The final scenario (Scenario 11) resulted in the maximum observable pressure increase (Fig. 4) and the resulting pressure field was output in 5 year time steps for input into the geomechanical model described below. In Scenario 11, the fracture pressure was exceeded at the shallow seabed outcrop and in cells immediately surrounding the injection wells in Bunter closures 39 and 40. Scenario 11 represents a conservative downside case, in which horizontal permeability (K_H) has been set to $0.65K_H$ in the base-case model to match the lower-bound permeability derived from pressure recovery data from the Esmond gas field (Bentham *et al.* 2017). The ratio of horizontal to vertical permeability ($K_V/K_H = 0.01$) has been reduced by an order of magnitude relative to the base case, and the NEP downside relative permeability curves modelled. The seabed outcrop is shut in this model, meaning no pressure relief. Finally, the BHP cutoff has been set to a nominal high value to allow the full amount of CO_2 to be injected at each well location.

Table 7. Total injected mass of CO_2 in each of the simulation runs expressed as a percentage of the target injected mass of 232 Mt

Simulation scenario run	Total injected mass (Mt)	Percentage target injected mass	Maximum percentage of fracture pressure
1	230.28	99.26	84.27
2	230.28	99.26	120.00*
3	230.37	99.30	84.85
4	230.37	99.30	133.10*
5	229.58	98.96	86.84
6	230.53	99.37	82.91
7	224.18	96.63	90.74
8	214.15	92.30	91.94
9	178.72	77.03	88.78
10	178.68	77.01	95.86
11	232.00	100.00	116.0†

The maximum pressure reached in the simulation expressed as a percentage of the fracture pressure is also shown for each scenario run.
*The fracture pressure is only exceeded at the shallow seabed outcrop (Fig. 1).
†The fracture pressure is exceeded at the seabed outcrop and in the vicinity of the injection wells.

Geomechanical model

Across the simulated scenarios, the Scenario 11 run resulted in the maximum modelled pressure increase (Fig. 4). Consequently, this scenario was taken forward to the geomechanical model to evaluate the geomechanical response corresponding to the worst-case pressure response. The resulting pressure field was output in 5 year time steps for input into the geomechanical model.

Geomechanical modelling was undertaken using the Visage simulator within the Petrel Reservoir Geomechanics workflow (Schlumberger 2017). The pressure responses from the Scenario 11 simulation results were imported into Petrel as time-attributed grid

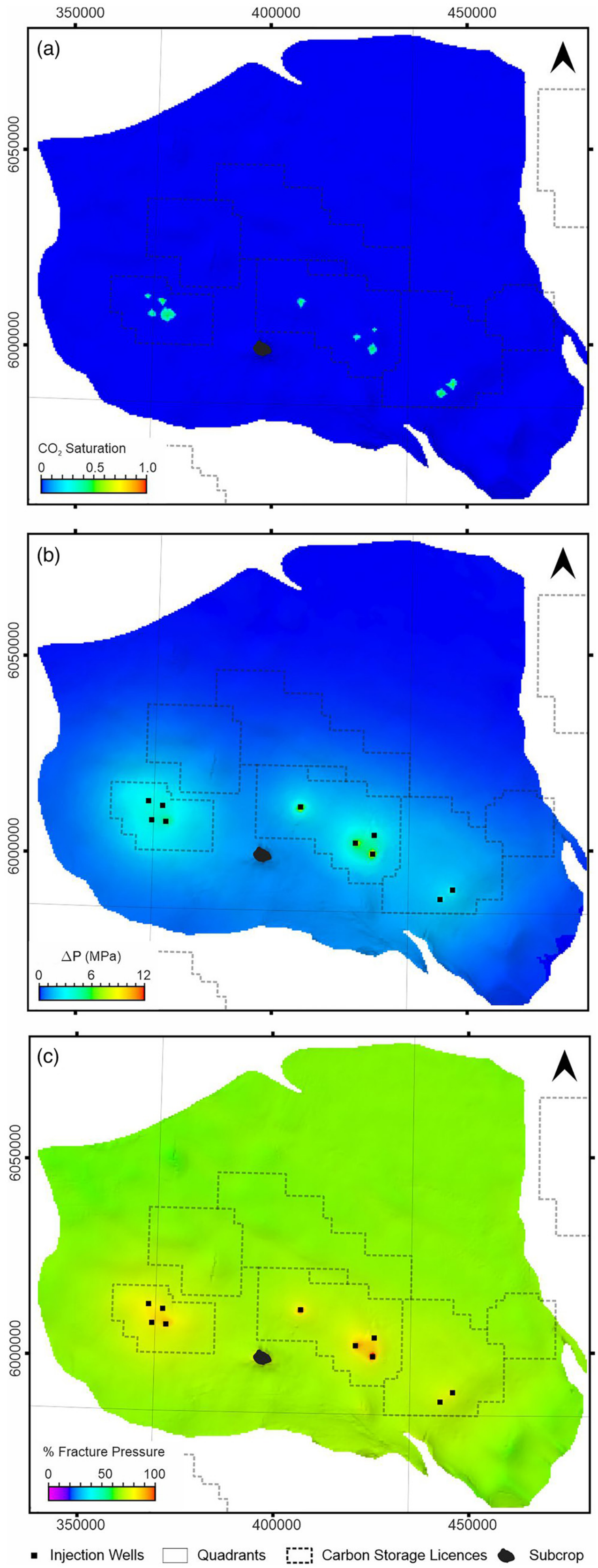

Fig. 4. Three-dimensional perspective view showing (**a**) the saturation distribution, (**b**) the pressure change (in MPa) and (**c**) the percentage of fracture pressure attained after 25 years of CO_2 injection for Scenario 11 run (100% CO_2 storage case in a lower quality Bunter Sandstone Formation reservoir). Note that in (c), the 'fracture pressure' was calculated using a gradient of 16.8 MPa km^{-1} based on fracture closure pressures from the Bunter Sandstone Formation at the Endurance site.

properties at 5 year intervals to enable one-way coupling with the geomechanical modelling simulator. Saturation and temperature effects were not considered in the regional model. However, results from a site-scale non-isothermal simulation model based on the Endurance site were later used to evaluate the potential extent of the thermal stress response and its implications for regional geomechanical responses.

The modelling process comprises the following steps:

- The model was initialized to calculate initial strains and intra-grid stresses at the first-time step (pre-injection), using a combination of pressure properties, boundary conditions and elastic properties defined in the geomechanical model.
- One-way coupling, where pressure outputs from the reservoir simulation were used to determine changes in rock strain, displacement and stress at 5 year time steps, using a linear elastic solver. Calculations on the mode of rock failure were also made for each cell at each step.

Two-way coupling with permeability updating was not undertaken due to a lack of input data relating porosity and permeability changes to pore pressure. A previous modelling study of CO_2 storage in an analogous setting suggested that the relatively benign nature of the storage site meant that results differed marginally between coupled models using generic rock mechanics data v. those using laboratory-derived data (Olden *et al.* 2012). A carefully designed experimental programme would be needed to enable fully coupled flow–geomechanical modelling to support future expansion of CO_2 injection into the Silverpit Basin.

Rock mechanical properties

The rock mechanical properties were bulk attributed to each stratigraphic unit in the model based on dominant lithology. As shown in Table 8, five discrete lithology identifiers were described in the model. Tertiary shale properties were assigned to all units between the seabed and the top of the Chalk Group. Properties are based on laboratory measurements taken from the Nordland Shale Formation at the Sleipner CO_2 storage site in the Norwegian North Sea (Zweigel and Heill 2003; Harrington *et al.* 2007). Chalk parameters were taken from the in-built geomechanical properties reference library included within the Visage package.

Halite, claystone and sandstone properties were derived from rock mechanical testing of Bunter Sandstone Formation, Röt Clay and Röt Halite samples reported in storage site development reports from the Endurance storage site (National Grid 2016*a*, *b*; BP 2021*a*). Although salt can exhibit both elastic and plastic behaviour, the halite units were modelled using an equivalent elastic medium approach, whereby Poisson's ratio was set to ensure a near-lithostatic stress state with low resulting shear stresses. The Young's modulus was then calculated from Poisson's ratio and the measured bulk modulus of *c.* 25 GPa (from logs). This approach ensures consistency between the parameters in the stress–strain calculations and is consistent with the modelling approach adopted by BP (2021*a*). Bulk densities for claystone and halite were tuned to ensure consistency between integrated log densities and modelled densities, given the coarse nature of the overburden elements in the 3D model. Biot's coefficient was set to unity for all units to maximize the impact of pressurization on the effective stress. This can be considered a worst-case scenario, providing a valid end-member approach for assessing the safety of a storage site in the absence of a comprehensive laboratory characterization study of the reservoir.

Table 8. Rock mechanical properties used in the geomechanical modelling

Property	Tertiary shale	Chalk	Claystone	Halite	Sandstone
Isotropic elastic properties					
Young's modulus (GPa)	1	7.5	13.8	0.75	14.5
Poisson's ratio	0.17	0.2	0.24	0.495	0.25
Density (g cm^{-3})	2	2.4	2.6	2.17	2.31
Biot's coefficient	1	1	1	1	1
Linear thermal expansion coefficient (LTEC) (1×10^{-5} °C^{-1})	1.3	1.3	1.4	4	1.2
Porosity	0.35	0.3	0.3	0	0.16
Mohr–Coulomb yield parameters					
Uniaxial compressive strength (MPa)	6	25.5	34.8	-	39.0
Friction angle (°)	45	41	36	-	36
Dilation angle (°)	22.5	20	18	-	18
Tensile strength cutoff (MPa)	0.6	0.7	4.1	-	3.9

Young's modulus and Poisson's ratio were tested under drained conditions.

In situ stress conditions

The geomechanical model was initialized to match key *in situ* stress observations, namely vertical stress and fracture closure pressure measurements from the Endurance site (Fig. 5). The following multistage process was used to generate optimized initialization stress inputs for the geomechanical model:

(1) Vertical stress was generated by vertical integration of formation bulk densities derived from the 3D geological model.
(2) Lithology-specific stresses for the sandstone- and claystone-dominated units were generated using gradients to fit the fracture closure pressures from the Bunter Sandstone Formation and Röt Clay. Lithostatic stresses were assigned to the halite units.
(3) Six-component stress results were concatenated from the lithology-dependent initialization runs to account for lithology-dependent stress variations.
(4) Optimized stress initialization was generated from explicit full-stress tensor inputs produced from the concatenated initialization results produced in the previous step.

Stress is a six-component tensor that, at depth, can be conveniently resolved into three principal components, one of which is the vertical stress (S_v) while the other two are horizontal and orthogonal to each other (Zoback *et al.* 2003). Vertical stresses were obtained from integration of bulk density logs from both the Endurance and BC36 sites. To generate the vertical stress input for the initialization of the geomechanical model, overburden densities were first assigned on a bulk basis to each stratigraphic unit based on the average formation densities as per Table 8. The vertical stress condition was then initialized by imposing boundary conditions to the model. In this mode the vertical stress is calculated from the integration of the density property from the 3D model and therefore accounts for stratigraphic thickness variations across the model. Overburden densities were carefully tuned to optimize the match between the integrated density logs from both sites, and vertical stress output from the model (Table 8). The magnitude of the maximum and minimum horizontal stresses ($S_{H\ max}$ and $S_{h\ min}$, respectively) are more difficult to obtain, but can be determined from small-scale hydraulic fracture tests in wells. Accurate fracture closure values were obtained for both the Bunter Sandstone Formation and the Röt Clay from minifrac testing in the 42/25d-3 well during appraisal of the Endurance site (BP 2021*a*). These provided the fracture pressure gradients for the sandstone and claystone units (16.8 and 19.4 MPa km^{-1}, respectively) that were used to initialize stresses in the geomechanical model (Fig. 5). In lieu of specific measurements, the lower sandstone stress gradients were applied to the Tertiary shales and the Chalk Group. This ensured an excellent match between the fracture pressure estimates for the Endurance site and the $S_{h\ min}$ magnitudes in the model.

As shown in Figure 5, the principal horizontal stress components are both lower than the vertical stress, corresponding

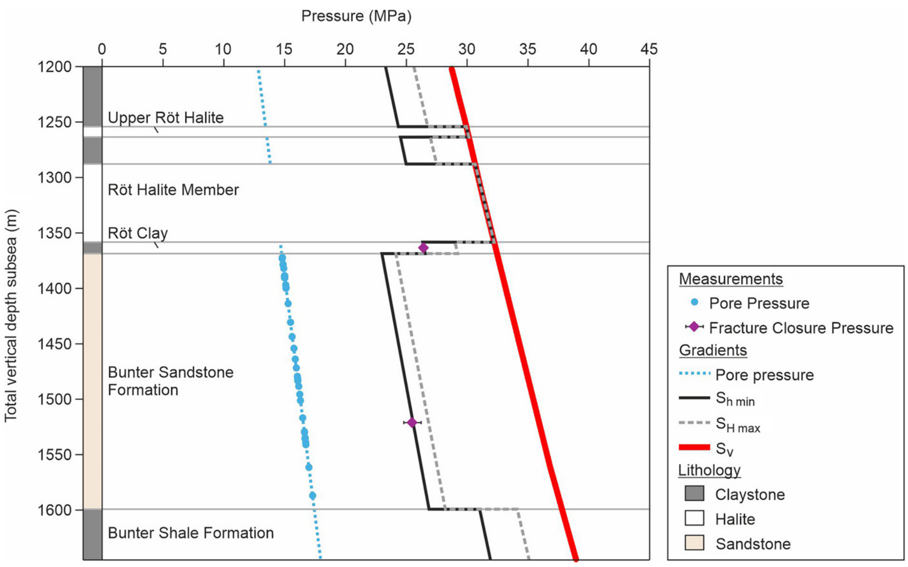

Fig. 5. Pressure and stress data from well 42/25d-3 at the Endurance storage site. Pore pressure data are derived from the modular formation dynamics tester (MDT), while fracture pressure data (average and range) are from the minifrac data reported by BP (2021*a*). The vertical stress was calculated by integration of the bulk density log. Source: contains information provided by the North Sea Transition Authority and/or other third parties (https://ndr.nstauthority.co.uk/).

to a normal stress regime as indicated by Williams *et al.* (2014, 2015) and confirmed by analysis of data from Endurance (BP 2021*b*). The magnitude of $S_{H\ max}$ was calculated from stress ratios based on analysis of sonic scanner logs reported by BP (2021*b*). This analysis suggests a $S_{H\ max}/S_{h\ min}$ ratio of 1.05 in the Bunter Sandstone Formation and 1.10 for the Röt Clay (Fig. 5). Lithostatic (isotropic) stress was assumed for the halite units (Röt Halite, Upper Röt Halite and Muschelkalk halite), where $S_{h\ min} = S_{H\ max} = S_v$.

For all non-halite units outside the extent of the reservoir flow simulation model, pore pressure was set to a gradient of 11 MPa km^{-1}. For halite units, pore pressure was set to zero, such that one of the terms in the effective stress calculation would be zero (given a Biot's coefficient of 1) and the halite would not contribute to the effective stress calculation.

It is likely that the presence of thick Zechstein Group evaporite sequences act to decouple the stress state in the supra-salt section from the tectonic stresses prevalent in the basement rocks (Williams *et al.* 2015). This notion is supported by the assessment that normal stress conditions prevail at the Endurance storage site, while strike-slip faulting conditions are suggested by the presence of drilling-induced tensile fractures in deeper rocks beneath the Zechstein Group evaporites. This has led to suggestions that whilst there is a strong NW–SE orientation of $S_{H\ max}$ in deeper strata, horizontal stress orientations in the supra-salt succession might potentially be more variable and relatable to local structures (Williams *et al.* 2015). The only reliable estimate of the $S_{H\ max}$ orientation from the supra-salt section at the Endurance site is based on dispersion analysis of sonic scanner logs. Some minor slowness anisotropy in the Bunter Sandstone Formation was identified, with the fast shear azimuth, assumed to be representative of $S_{H\ max}$, orientated between 92° and 105° (BP 2021*a*). This orientation is displayed over the top reservoir map for the site in Figure 6, which shows that it is approximately perpendicular to the contours. It is unclear if the stress orientations elsewhere on the structure will have a similar orientation, or if they will bear a similar relationship to local dip. Owing to the lack of data, a constant $S_{H\ max}$ of 148° is used for the geomechanical modelling, equal to the average orientation of $S_{H\ max}$ calculated from borehole breakouts in the UK SNS (after Williams *et al.* 2015). The orientation of $S_{H\ max}$ is not expected to impact the geomechanical modelling due to a lack of explicitly defined faults in the model, and the relaxed nature of the stress conditions at the site.

Geomechanical results

Strain

Modelled strains throughout the injection period and at the cessation of injection, when pressure was at its greatest, are very low, with some negative (dilational) strains modelled in the Bunter Sandstone Formation, Röt Clay and Bunter Shale and even lower positive (contractional) strains in the overburden and underlying strata (Fig. 7). While the dilational strains resulted directly from pressure changes in the reservoir, the contractional strains result from the consequent compressive stresses in the surrounding strata caused by reservoir expansion. The magnitude of the dilational strains rarely exceed -5×10^{-4} and contractional strains are limited to 1×10^{-4}. Note that contractional strains are signed positive and dilational strains are negative in the Visage package. Contractional strains in the Zechstein Group evaporites, particularly evident beneath BC39 and BC40, potentially acted to reduce strain transmission to the overburden. The thinner Triassic halite layers of the Röt and Muschelkalk members in the top seal experienced the greatest contractional strains due to their mechanical weakness and ductile behaviour.

Stress paths and failure

The most significant pressure changes are experienced in the vicinity of the injection wells at each of the sites, with the highest pressure changes observed at BC39, which is outside the seismic PRP where reservoir porosity and permeability are reduced. Mohr circle and stress path plots for modelled elements in the uppermost Bunter Sandstone Formation at the Endurance site and BC39 are shown in Figure 8. The plots indicate that the stress state does not exceed the strength of the intact material at any point throughout the injection period. The stress path for the Bunter Sandstone Formation follows an approximately linear trajectory owing to the porous and relatively permeable nature of the material. Within the Bunter Sandstone Formation, the increase in pressure reduces the effective stress and causes progressive displacement of the Mohr circle towards the failure envelope and closer to failure. Simultaneously, however, the coupled nature of pore pressure and stress (Hillis 2000) results in poro-elastic effects that increase the horizontal stresses relative to the vertical stress. Being in a normal stress state (where $S_v > S_{H\ max} > S_{h\ min}$), this results in a reduction in the differential stress and in the size of the Mohr circle. The stress path therefore moves approximately

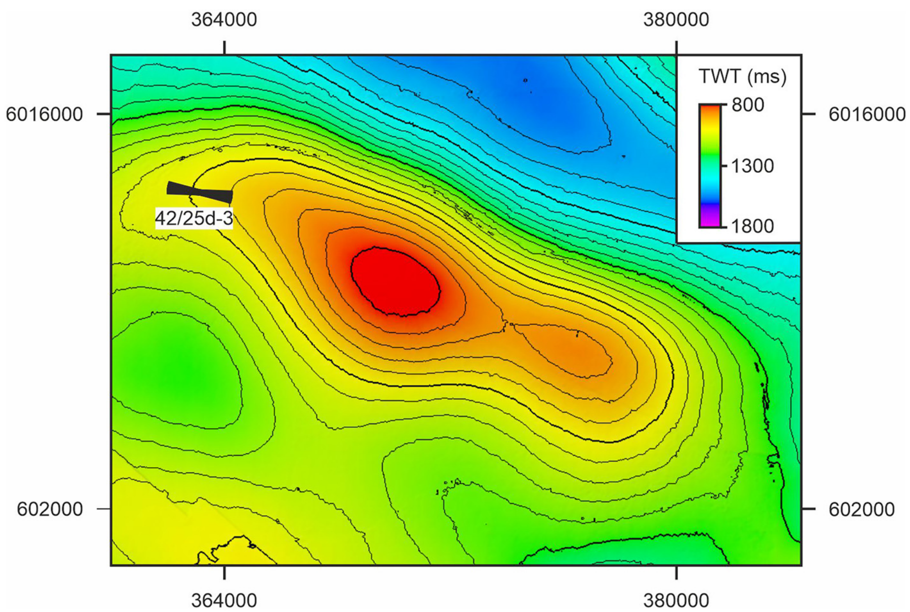

Fig. 6. Two-way travel time (TWT) structure at the top Bunter Sandstone Formation level at the Endurance structure. Interpreted $S_{H\ max}$ orientation derived from dispersion analysis of sonic scanner logs from well 42/25d-3, shown by the rose diagram at the well location. Source: after BP (2021*a*); the seismic data were provided by SLB.

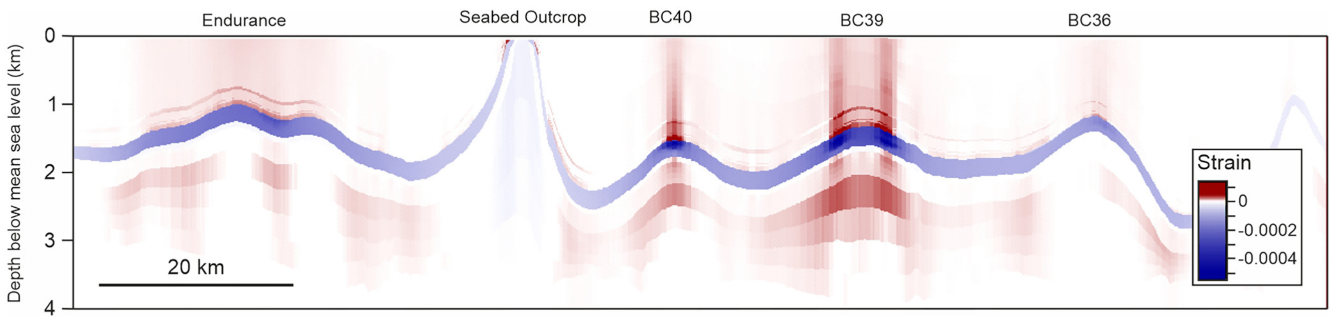

Fig. 7. Vertical elastic strain distribution (dimensionless) along a cross-section through the geomechanical grid at cessation of CO_2 injection in 2051. The line of the cross-section is shown in Figure 1 and is consistent with the geological section shown in Figure 3. Note the non-linear colour scale to highlight the very low positive (contractional) strains in the overburden and underlying strata.

parallel relative to the failure envelope. For extensive reservoirs with high width/height ratios, such as the Bunter Sandstone Formation, this effect partially counteracts the impact of the effective stress reduction, as recognized by Williams *et al.* (2016). Consequently, the stress state remains stable and failure is avoided, despite relatively high elevated pore pressures (P_p) (Fig. 8). Stress path values ($A = \Delta S_{h\,min}/\Delta P_p$) for both cases are indicative of stable conditions as they are less than 0.67, which is the value at which production-induced normal faulting would be expected to occur for a typical coefficient of friction of 0.6 (Chan and Zoback 2002). Elastic properties within the model were bulk attributed due to the regional scale of the model. Although variability in elastic properties would be expected to impact the modelled stress paths, a Biot' coefficient of unity means that the sensitivity to elastic properties is secondary to the strong poro-elastic effects. Analysis of the sensitivity to elastic properties is suggested for future site-scale modelling activities.

In the injection scenario modelled, injection does not commence at BC39 until 2029, so the significant initial effective stress reduction between 2026 and 2031 reflects a sharp increase in pressure resulting from the onset of injection to a relatively low-permeability aquifer (as part of the closure lies in the zone of reduced permeability outside the seismic PRP). Pressure subsequently increases at a lower rate once the initial relative permeability constraints are overcome. The pressure change observed prior to commencement of injection at BC39 is

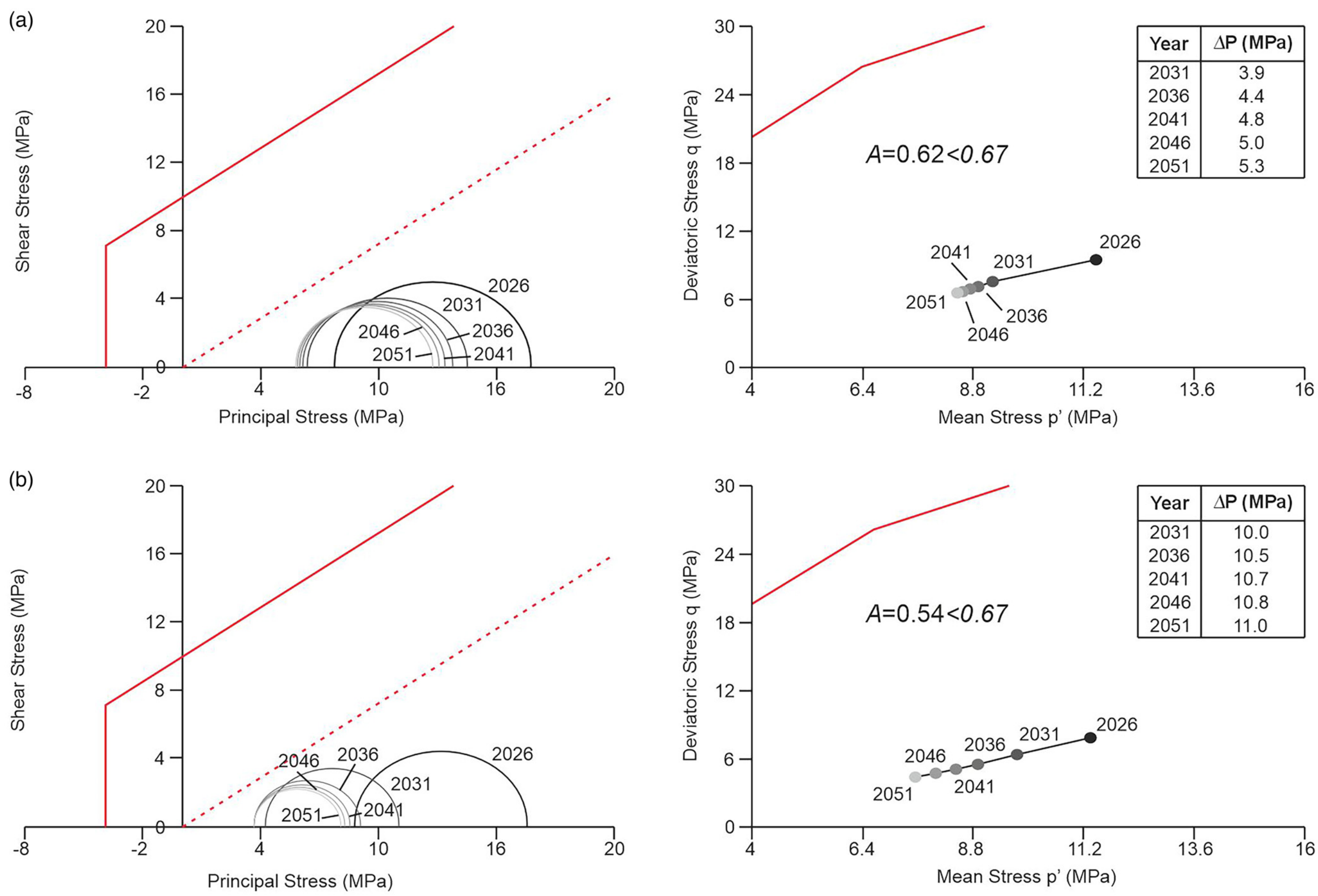

Fig. 8. Mohr circle and mean stress (p')–deviatoric stress (q) path plots illustrating the evolution of stress in the uppermost Bunter Sandstone Formation beneath the top seal at the locations of highest pressure increase at (**a**) the Endurance site and (**b**) at BC39. The solid red line delimits the failure envelope for intact rock, whereas the broken red line passing through the origin defines the failure envelope for cohesionless fault materials. The tables show the change in pressure at each time step relative to initial conditions. Stress path values are denoted by A and are less than 0.67, the value at which production-induced normal faulting would be expected to occur.

limited to *c.* 0.011 MPa, indicating that prior to injection at BC39 the structure experiences minimal impact from the earlier onset of injection at the Endurance site.

To account for the lack of explicitly represented faults in the model, the plots in Figure 8 also show failure envelopes for a cohesionless fault material. No failure would be expected, even given this conservative assumption. This contrasts with earlier estimates of fault-reactivation pressures derived from a static analysis using regional pore pressure and stress gradients where poro-elastic effects are neglected (Williams *et al.* 2014).

Vertical displacement

Maximum vertical displacement (uplift) is *c.* 0.12 m within the Röt Halite Member above BC39, where the greatest displacement is observed due to pressure build-up in the lower permeability reservoir. This corresponds to a maximum uplift of the overlying seabed of *c.* 0.09 m (Fig. 9). The modelled uplift at this site results from increased dilational strains within the Bunter Sandstone Formation associated with the lower porosity and permeability outside the seismic PRP.

Figure 10 illustrates the spatial extent of the modelled surface displacements in map view. Whilst spatially extensive, the magnitude of uplift is relatively low and significant tilting of the seabed does not occur. Whilst uplift is expected to be experienced by any infrastructure attached to the seabed, the low magnitude of the uplift suggests that adverse impacts on the stability of surface structures, such as wind turbines, are likely to be negligible. One interesting aspect of the spatial distribution of uplift is that the underlying structural accumulations of the Bunter Sandstone Formation are revealed from the displacement map, even in the case of structural accumulations where CO_2 is not injected. This effect is likely to stem from the reduced overburden thickness above the structural highs, reducing the effect of the contractional strains in the overburden, which otherwise partially counter the positive (upward) surface displacement caused by dilation of the Bunter Sandstone Formation reservoir

Although of similar magnitude, modelled surface displacements are slightly lower than those observed in published site-specific modelling studies of the Endurance site and BC36 structures (ETI 2016; National Grid 2016*a*; BP 2021*a*). This is interpreted to result from the larger hydraulically connected pore volume considered in this work, which is based on a structural analysis of regional pressure boundaries (Abel *et al.* 2025). The larger connected pore volumes in our model enable further dissipation of the increased pressures into the formation, somewhat limiting the localized pressure increases proximal to the injection sites. This supports the finding of Olden *et al.* (2012) that realistic and accurate pressure-response prediction is the most important aspect in modelling induced geomechanical responses in large saline aquifer storage systems. Effective pressure dispersion in large, connected saline aquifer formations essentially serves to ameliorate the potentially negative geomechanical impacts at the injection sites.

Thermal stress effects

Piped CO_2 is likely to arrive at the well perforations at a temperature significantly below the ambient reservoir temperature. Injection of a fluid that is cooler than the reservoir may induce thermal fracturing of the reservoir. Fracturing of the top seal is also possible should the temperature anomaly extend vertically into the overburden. A refined reservoir model of the Bunter Sandstone Formation formation and overlying cap rock locally covering the Endurance site structure was built to assess the impact of reservoir cooling on geomechanical stability. Reservoir properties were assigned as per the regional model (Table 3), while overburden properties were assigned the values shown in Table 4. Rock thermal properties were assigned to each lithology, as summarized in Table 4.

For this non-isothermal test case, 4 Mt of CO_2 per annum was injected into the Endurance structure through four wells (Fig. 1). The seabed temperature in this part of the UK SNS ranges from *c.* 4 to 15°C (ETI 2016; National Grid 2016*a*). Here, we model a downside scenario in which the enthalpy of the injected CO_2 is calculated for a wellhead temperature and pressure of 4.3 MPa and 4.0°C, respectively, representing injection during a winter minimum. The results show that the injected CO_2 cools an area of reservoir with a diameter of *c.* 825 m immediately surrounding the injection wells (Fig. 11). The low-temperature plume also extends into the overburden, to a height of *c.* 70 m, impacting the Röt Clay and the overlying Röt Halite. The maximum observed temperature drop at the well perforations is *c.* 50°C, reducing the reservoir temperature to *c.* 8°C. Cooling of *c.* 15°C is observed in the Röt Halite. These results are comparable with a modelled reservoir temperature of 11°C published by BP (2021*b*) and of 15°C by National Grid (2016*a*) immediately surrounding the injection well perforations. The area influenced by the thermal plume is also similar in extent to the results of McDermott *et al.* (2016), who evaluated the thermal and mechanical stability of the Captain Sandstone saline aquifer as an example of another potential shared multi-user CO_2 storage asset.

The non-isothermal pressure and temperature results were used as input into a coupled geomechanical model simulation. The stress initialization and coupled modelling procedures were similar to those used for the isothermal regional model, albeit with a different (site-scale) input grid, single-site injection scenario and inclusion of thermal stress effects.

Cooling of the Bunter Sandstone Formation reservoir results in contractional strains that are particularly prevalent within a *c.* 300 m radius of the injection wells but which diminish rapidly with distance from the wellbore thereafter (Fig. 11). The magnitude of the contractional strains was very low – of the same magnitude as the dilational strains experienced in the isothermal models. Despite the

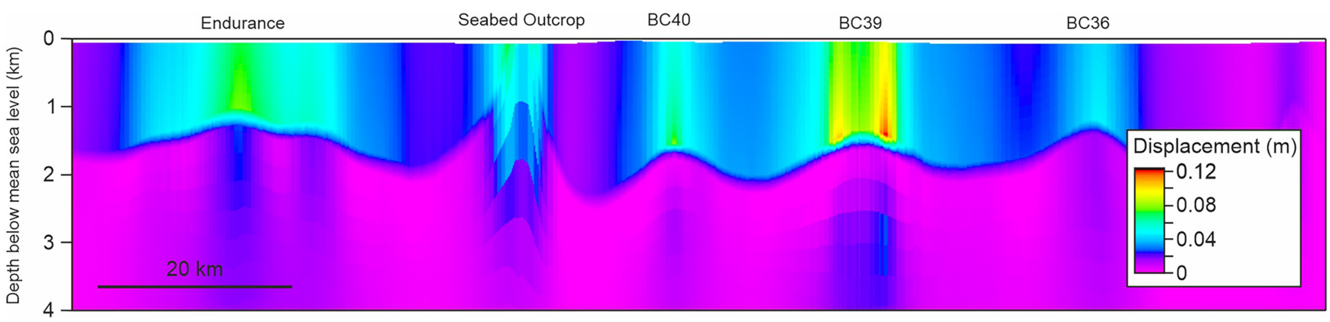

Fig. 9. Cross-section showing the vertical displacement in metres (linear solver) through the geomechanical grid at cessation of CO_2 injection in 2051. The depth is in kilometres. The line of the cross-section is shown in Figure 1 and is consistent with the geological section shown in Figure 3.

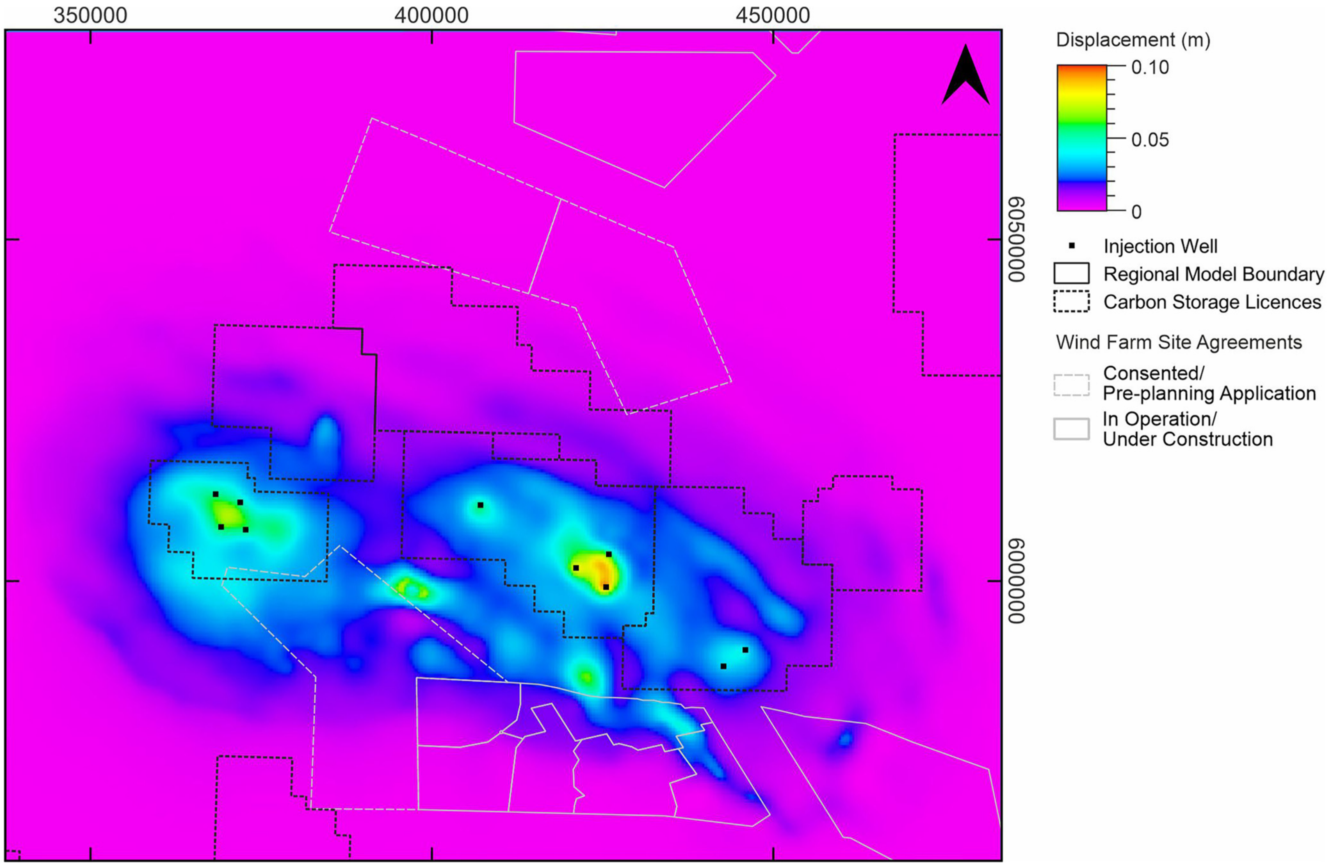

Fig. 10. Map view showing the modelled surface displacements in relation to wind farm leases and carbon storage licences. Source: the carbon storage licence linework contains information provided by the North Sea Transition Authority and/or other third parties (https://opendata-nstauthority.hub.arcgis.com/search?collection=Dataset); the wind farm outlines contain data provided by The Crown Estate that is protected by copyright and database rights (https://opendata-thecrownestate.opendata.arcgis.com/).

modest temperature reductions (10–20°C) in the overlying Röt Halite, thermally induced strains are high due to the high linear thermal expansion coefficient (LTEC) of the halite (Table 8). This did not result in failure of the cap rock under modelled temperature and pressure conditions; however, this effect was previously identified as a potential risk by ETI (2016). Consequently, it was recommended that CO_2 be injected in the lower part of the Bunter Sandstone Formation to minimize the cooling effect at the interface between the reservoir and the top seal (ETI 2016). The wells are located such that there is no constructive interference of thermal plumes that could otherwise result in a cumulative bulk cooling effect of the storage site or the cap rock. Outside of the *c*. 825 m radius of influence, changes in stress and strain are sensitive to pressure changes only.

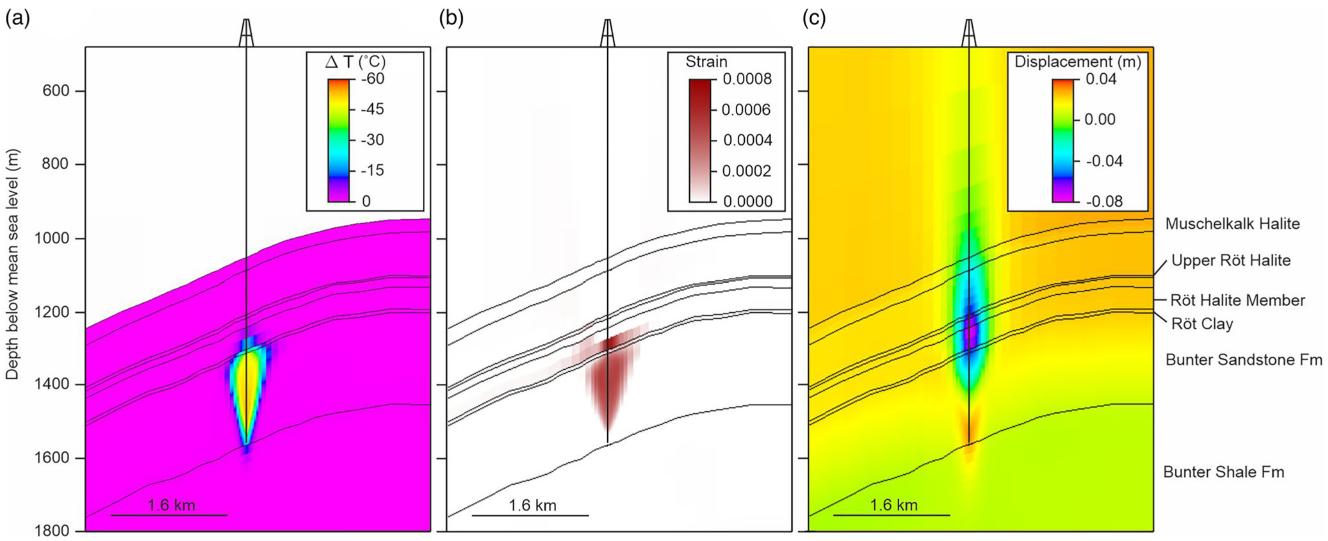

Fig. 11. (**a**) Temperature change (ΔT), (**b**) vertical strain and (**c**) vertical displacement around one of the Endurance injection wells at the end of the injection period in 2051.

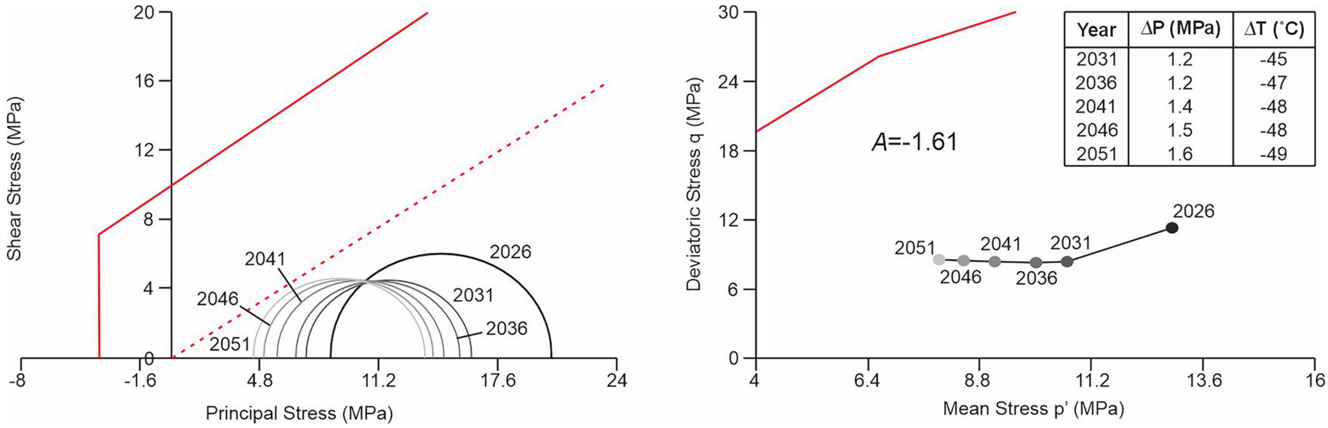

Fig. 12. Mohr circle and mean stress (p')–deviatoric stress (q) path plot illustrating the evolution of stress in the uppermost Bunter Sandstone Formation beneath the top seal at the location of one of the Endurance injection wells in the non-isothermal reservoir simulation. The solid red line delimits the failure envelope for intact rock, whereas the broken red line passing through the origin defines the failure envelope for cohesionless fault material. The table shows the change in pressure and temperature at each time step relative to initial conditions.

While failure is not experienced at any point in the model, the stress path is clearly evolving towards the failure state (Fig. 12). Consequently, shear failure might be anticipated if any critically stressed faults or fractures are present given the proximity of the stress state to the failure envelope at the end of injection period in 2051 (Fig. 12). Note that the lower Δ*P* values indicated in Figure 12 relative to Figure 8 arise from differences in the handling of numerical aquifer volumes in the local model relative to the regional model.

The net impact of the thermal contraction is that subsidence of the order of *c.* 8 cm is expected to occur immediately above the reservoir in the vicinity of the injection wells (Fig. 11). As a result, the uplift at the seabed in the vicinity of the injection wells is likely to be somewhat reduced relative to the isothermal case presented in Figures 9 and 10. This may negate any potential impact of seabed uplift on surface structures such as well platforms and injection infrastructure directly above the injection point.

A detailed well injectivity and fracture modelling study was conducted in support of the commercial appraisal process for the Endurance storage site (BP 2021*c*). In contrast to the results reported here, the BP (2021*c*) analysis suggested that thermally induced fracturing of the Bunter Sandstone Formation would occur. Despite this, none of the modelling cases presented indicated that induced fractures would reach the top of the reservoir. The risk of vertical fracture growth was therefore considered to be manageable, with a low risk that CO_2 would move vertically along fractures to the top of the reservoir (BP 2021*c*). Whilst thermal stress impacts are clearly important in the context of CO_2 storage in saline aquifers, impacts are local in nature and, in the case of the Bunter Sandstone Formation, associated CO_2 containment risks can be managed through effective well design and injection control.

Discussion

Boundary conditions

Based on the structural study of Abel *et al.* (2025), this study considered the Silverpit Basin, bounded by the Dowsing Graben System, North Dogger Fault Zone, Outer Silverpit Fault Zone and the East Silverpit Fault Zone, to comprise a large, yet closed, hydraulic volume. This is a key assumption in the model, as the connected aquifer volume is very large, enabling effective dissipation of pressure away from the injection sites and allowing for a sustained injection schedule to be maintained. Although pressure data collected during legacy exploration and appraisal activities provide compelling evidence in support of this, Abel *et al.* (2025) suggest that pressure communication across the East Silverpit Fault Zone might be possible. Although this would provide a further upside in terms of connected aquifer volume, connection with the eastern portion of the basin could result in displacement of brine across the international boundary and into the Dutch sector. The potential for cross-border pressure perturbations associated with CO_2 storage in the Bunter Sandstone Formation has previously been investigated by Hannis *et al.* (2013), and are likely to require bilateral discussions between regulatory agencies.

Prior simulation studies (i.e. Noy *et al.* 2012) have considered the impact of the seabed outcrop on pressure increases during CO_2 storage in the Bunter Sandstone Formation. The outcrop is a key feature, as it enables a degree of pressure alleviation through release of brine to the water column, whereas the CO_2 remains structurally trapped within the closures. Along with the BHP constraints applied to the injection wells, the outcrop provides mitigation against unacceptable pressure increases in the model. While this effect is enabled in most of the reservoir simulations presented, communication with the outcrop is deactivated in the scenario taken forward in the geomechanical modelling. Despite the lack of pressure alleviation via the outcrop, the full target mass was injected without inducing any negative geomechanical impacts. This is enabled due to the low height/width ratio (*c.* 0.00125) of the reservoir based on a mean thickness of 168 m and cross-sectional length of 134 km. During fluid injection, horizontal stresses increase due to subsurface confinement, whereas the free Earth surface prevents significant changes to the vertical stress. The consequence of the horizontal stress change is that the stress path moves approximately parallel to the failure envelope (Fig. 8). Under the modelling assumptions presented, shear failure is unlikely to occur in the absence of a critically stressed fault subjected to a very significant increase in pore pressure. Failure of intact rock would be more likely to occur in tensile mode; however, this would also require severe pore pressure increase.

A major assumption underpinning the modelling is that the Bunter Sandstone Formation within the Silverpit Basin is not internally compartmentalized due either to structural or sedimentological factors. If the reservoir is unexpectedly compartmentalized, pressure might rapidly build-up more locally. The presence of any regionally significant baffle to porewater redistribution could change the geometry of the effective reservoir, potentially developing a thick, localized, laterally restricted reservoir compartment. This would reduce the impact of the change in horizontal stress magnitude relative to the vertical stress during fluid injection. This risk would be mitigated by careful siting of injection wells to avoid zones of structural complexity, such as seismically resolvable faults.

The high NTG ratio and heavily reworked nature of the Bunter Sandstone Formation sediments means that primary sedimentary structures are poorly preserved (Gibson-Poole *et al.* 2024). Reservoir properties are therefore likely to vary over short length scales, and extensive permeability barriers are likely to be rare or absent. Downhole pressure monitoring would also be expected to be deployed during operation, enabling monitoring of pressure at the injection wells and allowing injection rates to be carefully managed. A requirement to reduce injection rates due to unanticipated pressure build-up may necessitate modifications to the development plan such that the required injection rates can be maintained. Pressure data acquired during injection will also allow ground-truthing of modelled pressure responses. The Snöhvit project is a good example of a CO_2 storage project that required a change of injection strategy because of unanticipated pressure build-up during injection, in that case resulting in a change in the injection interval (Hansen *et al.* 2013; Grude *et al.* 2014).

Another aspect of relevance to boundary conditions is the inclusion of overlying and underlying shale horizons (Röt Clay and Bunter Shale Formation) in the simulation model, rather than treating these as non-net inactive cells. Noy *et al.* (2012) showed that even very low top seal permeabilities can result in significantly reduced pressure footprints in the Bunter Sandstone Formation by enabling dissipation of brine into the surrounding rocks. Given the thin nature of the Röt Clay, its contribution to the pressure response is likely to be small; however, the underlying Bunter Shale Formation is far thicker. Although the pressure increase modelled in the Bunter Shale Formation is relatively low, the overall effect is to reduce the magnitude of the pressure increase in the reservoir. This has previously been shown in other saline aquifer CO_2 injection simulation models (i.e. McDermott *et al.* 2016).

Monitoring implications

Pre-injection geomechanical models form part of the appraisal process for CO_2 storage projects, helping to inform operational limits and monitoring plan development. Models are frequently subject to multiple uncertainties due to the relative scarcity of data relating to *in situ* stress and mechanical input parameters. This uncertainty can be particularly prevalent in saline aquifer storage settings. Monitoring throughout the project life cycle should provide observational data that can be used to validate and iteratively update pre-injection models. The application of monitoring data in CO_2 storage projects has provided valuable information relating to the performance of several commercial-scale CO_2 storage developments worldwide (Verdon *et al.* 2013; Goertz-Allmann *et al.* 2024).

Reservoir pressure and temperature can be effectively monitored both during and following the injection phase by instrumenting injection and monitoring wells with downhole gauges. Given the extensive nature of the pressure footprint, which is likely to extend beyond the storage licences, it would also be useful to monitor pressure in the far field. This would allow detection of any geomechanical impacts, whilst also enabling validation of numerical simulation models. However, the benefits would need to be balanced against the considerable cost of drilling additional monitoring wells. Alternatively, where multiple CO_2 storage projects are operating concurrently, the overall aquifer pressure responses might be better understood through data sharing arrangements. Other monitoring methods that may provide some insight into the regional pressure and associated geomechanical responses include time-lapse seismic methods, from which stress and strain changes in the subsurface can be determined. In principle, these surveys could be conducted in 1D, 2D or 3D modes using discrete or permanent arrays. However, the time-lapse changes associated with the very small strains computed in this study are likely to fall well below the noise threshold of conventional seismic survey technology available for offshore settings. Permanent reservoir monitoring (PRM) systems may be capable of resolving these very small strains; however, such systems would most likely be deployed locally to the injection sites where saturation changes dominate the time-lapse seismic response.

One deformation aspect that can potentially be monitored effectively is the surface elevation change resulting from uplift induced by dilational strains resulting from pressurization of the aquifer. Interferometric synthetic aperture radar (InSAR) was used successfully at the In Salah storage operation in Algeria (Vasco *et al.* 2008; Onuma and Ohkawa 2009). Surface displacements of the order of 1–2 cm were observed as a consequence of pressure increases of up to 12 MPa (Verdon *et al.* 2013). The onshore, isolated desert conditions provided ideal conditions for InSAR and contributed to the success of geodetic monitoring at In Salah, although use of InSAR methods would be particularly challenging in offshore storage settings such as the Bunter Sandstone Formation. Tiltmeters and/or global positioning systems (GPSs) attached either to the seabed or to structures anchored to the seabed, may provide sufficient information to detect surface elevation changes. Tiltmeters can also be implemented in boreholes (Gebauer *et al.* 2007). High-resolution bathymetric surveys or submersible pressure transducers might also possibly be of service in detecting subtle changes to seabed elevation changes. It is worth noting that natural changes to seafloor conditions over the injection period, such as the migration of sand bars, could result in far more substantive changes relative to the modest uplift effects indicated by the geomechanical model, potentially posing a challenge for seabed monitoring deployments.

Advancements in fibre-optic sensing have led to consideration of both surface and downhole fibres in CO_2 storage monitoring schemes (Furre *et al.* 2020; Pevzner *et al.* 2021; Tsuji *et al.* 2021). Fibre-optic sensing can be used to monitor CO_2 storage operations in several ways, including distributed temperature sensing (DTS), distributed acoustic/strain sensing (DSS/DAS) and seismic imaging, in addition to detection of microseismic events. Whereas pressure and temperature can only be inferred from DAS data using a combination of quantitative and qualitative interpretation, DSS/DAS systems provide an almost direct measurement of the strain affecting the fibre-optic cable. DSS/DAS technologies therefore show promising potential for monitoring the geomechanical response of the subsurface to CO_2 injection in real time, enabling verification of predictive geomechanical models. The significant volumes of data that would be generated pose a significant challenge, particularly in the case of continuous real-time monitoring. Planned field deployments in offshore storage settings (i.e. Furre *et al.* 2020) will provide insights into the practicality of exploiting DSS/DAS systems for the monitoring of CO_2 storage in offshore saline aquifers such as the Bunter Sandstone Formation. Downhole fibres deployed in injection wells or in dedicated monitoring wells may be required to monitor very small strains as modelled in this study.

Microseismic monitoring has proven to be valuable in monitoring deformation associated with fluid injection projects, including CO_2 storage operations (Verdon *et al.* 2013; Dando *et al.* 2021). Permanent passive seismic monitoring systems, whether using seismometers or fibre-optic systems, may be useful in detecting microseismicity associated with fault reactivation. The study area in the Silverpit Basin is bounded on all sides by major fault zones, therefore, in principle, there may be a concern that the far-field pressure response could result in felt seismicity at these structurally complex zones. It is important to note, however, that the magnitude of the pressure increase at the model boundaries simulated in this study are well below the threshold required to induce shear failure at the faulted boundaries. Likewise, localized crestal faulting over shallow structural accumulations will be more prone to reactivation relative to those at the injection sites because of the convergence of the hydrostatic and fracture pressure gradients towards the surface. Again, failure does not occur anywhere in the model under the current modelling assumptions. This is notable given that the geomechanical model was implemented using the simulation results that gave rise to the greatest increases in pore pressure. Regional seismicity therefore is not anticipated to result from deployment of the modelled injection schedule in the Bunter Sandstone Formation, although there may be a requirement for microseismic monitoring close to the injection sites.

Conclusions

- Coupled flow–geomechanical modelling indicates that, under the modelled loads, increasing reservoir pressure will generate only minor uplift and some minor elastic strain with no shear or tensile failure of the reservoir, top seal or overburden. Even under a conservative case with failure envelopes representative of optimally orientated, cohesionless materials, no failure is observed in either the Bunter Sandstone Formation or its top seals. This picture might change if unexpected compartmentalization of the saline aquifer leads to a smaller hydraulic unit volume.
- Following injection, it will be important to revisit pre-injection geomechanical models once additional information is acquired from monitoring datasets. For example, microseismic studies have identified seismicity along previously unidentified faults at other large-scale fluid injection projects.
- Although the thermal model did not result in failure, it suggests that thermally enhanced fracturing of the cap rock and potential for fault/fracture reactivation presents the greatest geomechanical containment risk.
- This risk is mitigated by the presence of a thick top seal succession and the creep potential of the Röt Halite. Operational factors such as careful siting of the injection location deeper in the reservoir and heating of the CO_2 stream can further mitigate the thermal fracture risk.
- Under current modelling assumptions the multi-store injection scenario considered in this study is feasible without inducing significant strain or failure in the Bunter Sandstone Formation or its top seal formations. Owing to the size of the connected aquifer volume, this conclusion is true even under conservative flow modelling assumptions.
- Dilation of the Bunter Sandstone Formation results in only modest uplift of the seabed (of the order of *c.* 10 cm), concentrated at the injection sites where pressure increases are greatest. Regionally, a small amount of uplift occurs over a wide area and is elevated above the salt-cored structural closures.
- The finding that the Bunter Sandstone Formation can accommodate injection of a significant volume of CO_2 without resulting in any negative geomechanical impacts confirms the results of published industry modelling studies. From a geomechanical perspective, the Bunter Sandstone Formation appears to be an excellent prospect for commercial-scale storage of CO_2.

Acknowledgements SLB are thanked for donating the Petrel, Eclipse and Visage software licences and for the provision of multi-client seismic data used for regional mapping. This paper is published with the permission of the Executive Director, British Geological Survey (NERC, UKRI).

Author contributions **JDOW**: formal analysis (lead), funding acquisition (lead), investigation (equal), methodology (lead), project administration (lead), supervision (lead), validation (equal), visualization (lead), writing – original draft (lead), writing – review & editing (equal); **GAW**: conceptualization (supporting), formal analysis (supporting), investigation (equal), methodology (supporting), validation (equal), visualization (supporting), writing – original draft (supporting), writing – review & editing (equal); **MWF**: investigation (supporting), writing – original draft (supporting); **LA**: visualization (supporting), writing – review & editing (supporting); **PB**: investigation (supporting), writing – review & editing (supporting).

Funding This work precipitated from initial studies undertaken during the ACT ELEGANCY project (Project No. 271498), which received funding from Federal Department of Environment, Transport, Energy and Communications (DETEC) (Switzerland), Federal Ministry for Economic Affairs and Energy (BMWi) (Germany), Rijksdienst voor Ondernemend Nederland (RVO) (The Netherlands), Gassnova (Norway), Business, Energy and Industrial Strategy (BEIS) (UK), Gassco, Equinor, and Total, and was co-funded by the European Commission under the Horizon 2020 programme (ACT Grant Agreement No. 691712). Funding was also provided by the Engineering and Physical Sciences Research Council (EPSRC) through the UK Carbon Capture and Storage Research Centre 2017 (grant No. EP/P026214/1 awarded to JDOW) and the Industrial Decarbonisation Research and Innovation Centre (IDRIC) (grant No. EP/V027050/1 awarded to JDOW). In addition, we acknowledge support from the Natural Environment Research Council (NERC) via the Managing the Environmental Sustainability of the Offshore Energy Transition (MOET) project (funded by the NERC National Capability Multi-Centre Science programme) and British Geological Survey National Capability funding. Characterization of the *in situ* stress conditions and consideration of monitoring implications were conducted during the SHARP Storage project (Project No. 327342), subsidized through ACT by RCN and Gassnova (Norway), RVO (The Netherlands), DST (India), BEIS (UK), and EUDP (Denmark).

Competing interests The authors declare that they have no known competing financial interests or personal relationships that could have appeared to influence the work reported in this paper.

Data availability The datasets generated during and/or analysed during the current study are not publicly available due to licencing constraints but are available from the corresponding author on reasonable request.

References

Abel, L., Williams, J.D.O. *et al.* 2025. Structural controls on pressure communication across the Bunter Sandstone Formation, UK Southern North Sea. *Geoenergy*, **3**, https://doi.org/10.1144/geoenergy2024-027

Agada, S., Jackson, S. *et al.* 2017. The impact of energy systems demands on pressure limited CO_2 storage in the Bunter Sandstone of the UK Southern North Sea. *International Journal of Greenhouse Gas Control*, **65**, 128–136, https://doi.org/10.1016/j.ijggc.2017.08.014

Allen, M.R., Griffiths, P.A., Craig, J., Fitches, W.R. and Whittington, R.J. 1994. Halokinetic initiation of Mesozoic tectonics in the southern North Sea: a regional model. *Geological Magazine*, **131**, 559–561, https://doi.org/10.1017/S0016756800012164

Armitage, P.J., Worden, R.H., Faulkner, D.R., Butcher, A.R. and Espie, A.A. 2016. Permeability of the Mercia Mudstone: suitability as caprock to carbon capture and storage sites. *Geofluids*, **16**, 26–42, https://doi.org/10.1111/gfl.12134

Batzl, M. and Wang, Z. 1992. Seismic properties of pore fluids. *Geophysics*, **57**, 1396–1408, https://doi.org/10.1190/1.1443207

Bennion, D.B. and Bachu, S. 2006. The impact of interfacial tension and pore-size distribution/capillary pressure character on CO_2 relative permeability at reservoir conditions in CO_2–brine systems. Paper SPE-99325-MS presented at the SPE/DOE Symposium on Improved Oil Recovery, April 22–26, 2006, Tulsa, Oklahoma, USA, https://doi.org/10.2118/99325-MS

Bentham, M., Mallows, T., Lowndes, J. and Green, A. 2014. CO_2STORage Evaluation Database (CO_2 Stored). The UK's online storage Atlas. *Energy Procedia*, **63**, 5103–5113, https://doi.org/10.1016/j.egypro.2014.11.540

Bentham, M., Williams, G., Vosper, H., Chadwick, A., Williams, J. and Kirk, K. 2017. Using pressure recovery at a depleted gas field to understand saline aquifer connectivity. *Energy Procedia*, **114**, 2906–2920, https://doi.org/10.1016/j.egypro.2017.03.1418

Blackbourn, G.A. and Robertson, L.F. 2014. *Sedimentology, Petrography and Burial History of the Cored Triassic Section in the National Grid Carbon Well 42/25d-3, UK North Sea*. Blackbourn Geoconsulting, Bo'ness, West Lothian, UK, https://ndr.ogauthority.co.uk/

BP 2021*a*. *Primary Store Geomechanical Model & Report*. Key Knowledge Document NS051-SS-REP-000-00012. Department for Business, Energy and Industrial Strategy, London, https://assets.publishing.service.gov.uk/media/6294fc258fa8f50398e15b8a/NS051-SS-REP-000-00012-Geomechanical_Model___Report-.pdf

BP 2021*b*. *Primary Store Dynamic Model & Report*. Key Knowledge Document NS051-SS-REP-000-00015. Department for Business, Energy and Industrial Strategy, London, https://assets.publishing.service.gov.uk/media/6294fca0d3bf7f037097bdc7/NS051-SS-REP-000-00015-Dynamic_Model___Report.pdf

BP 2021*c*. *Endurance Well Injectivity Fracturing Study with REVEAL*™. Key Knowledge Document NS051-SS-REP-000-00017. Department for Business, Energy and Industrial Strategy, London, https://assets.publishing.service.gov.uk/media/6294fcb3d3bf7f037097bdc8/NS051-SS-REP-000-00017-Well_Injectivity_TF.pdf

BP 2022. *Alternative Stores and Notional Development Plan*. Key Knowledge Document NS051-SS-REP-000-00022. Department for Business, Energy and Industrial Strategy, London, https://assets.publishing.service.gov.uk/media/6295281be90e070394dbc161/NS051-SS-REP-000-00022-Alt_Stores___Notional_Dev_Plan.pdf

Brennan, C. and Adam, J. 2023. Regional variability of onset and cessation of salt tectonics in the Mesozoic and Cenozoic Southern North Sea subbasins. *AAPG Bulletin*, **107**, 2169–2196, https://doi.org/10.1306/08072221105

Brennan, C., Preiss, A. and Adam, J. 2023. Three-dimensional seismic classification of salt structure morphologies across the Southern North Sea. *AAPG Bulletin*, **107**, 2141–2167, https://doi.org/10.1306/08072221136

Brooks, R.H. and Corey, A.T. 1964. *Hydraulic Properties of Porous Media*. Hydrology Papers, **3**. Colorado State University, Fort Collins, CO.

Bump, A.P. and Hovorka, S.D. 2023. Minimizing exposure to legacy wells and avoiding conflict between storage projects: exploring area of review as a screening tool. *International Journal of Greenhouse Gas Control*, **129**, https://doi.org/10.1016/j.ijggc.2023.103967

Bump, A.P. and Hovorka, S.D. 2024. Pressure space: the key subsurface commodity for CCS. *International Journal of Greenhouse Gas Control*, **136**, https://doi.org/10.1016/j.ijggc.2024.104174

Cameron, T.D.J., Crosby, A., Balson, P.S., Jeffery, D.H., Lott, G.K., Bulat, J. and Harrison, D.J. 1992. *United Kingdom Offshore Regional Report: The Geology of the Southern North Sea*. HMSO for the British Geological Survey, London.

Chan, A.W. and Zoback, M.D. 2002. Deformation Analysis in Reservoir Space (DARS): A simple formalism for prediction of reservoir deformation with depletion. Paper SPE-78174-MS presented at the SPE/ISRM Rock Mechanics Conference, October 20–23, 2002, Irving, Texas, USA, https://doi.org/10.2118/78174-MS

Corey, A.T. 1954. The interrelation between gas and oil relative permeabilities. *Producers Monthly*, **19**, 38–41.

Dando, B., Goertz-Allmann, B., Kühn, D., Langet, N., Dichiarante, A. and Oye, V. 2021. Relocating microseismicity from downhole monitoring of the Decatur CCS site using a modified double-difference algorithm. *Geophysical Journal International*, **227**, 1094–1122, https://doi.org/10.1093/gji/ggab255

De Luca, M., Mackay, E.J., Good, T.R., Scisciani, V., MacBeth, C., Patruno, S. and Sutcliffe, J. 2025. Regional pressure response to large-scale carbon storage in the bunter sandstone formation, Silverpit Basin (Southern North Sea, UK). *International Journal of Greenhouse Gas Control*, **148**, https://doi.org/10.1016/j.ijggc.2025.104530

Doornenbal, H. and Stevenson, A. (eds) 2010. *Petroleum Geological Atlas of the Southern Permian Basin Area*. European Association of Geoscientists and Engineers (EAGE), Houten, The Netherlands.

Doornenbal, J.C., Kombrink, H. *et al.* 2022. New insights on subsurface energy resources in the Southern North Sea Basin area. *Geological Society, London, Special Publications*, **494**, 233–268, https://doi.org/10.1144/SP494-2018-178

Duan, Z. and Sun, R. 2003. An improved model calculating CO_2 solubility in pure water and aqueous NaCl solutions from 273 to 533 K and from 0 to 2000 bar. *Chemical Geology*, **193**, 257–271, https://doi.org/10.1016/S0009-2541(02)00263-2

Duan, Z., Hu, J., Li, D. and Mao, S. 2008. Densities of the CO_2–H_2O and CO_2–H_2O–NaCl systems up to 647 K and 100 MPa. *Energy & Fuels*, **22**, 1666–1674, https://doi.org/10.1021/ef700666b

ETI 2016. *D10: WP5A – Bunter Storage Development Plan*. Report 10113ETIS-Rep-13-03. Prepared by Pale Blue Dot Energy & Axis Well Technology. Energy Technologies Institute (ETI), Loughborough, UK, https://ukerc.rl.ac.uk/publications/technical_report/CCS_CC1026_8.pdf

Furnival, S., Wright, S., Dingwall, S., Bailey, P., Brown, A., Morrison, D. and De Silva, R. 2014. Subsurface characterisation of a saline aquifer cited for commercial scale CO_2 disposal. *Energy Procedia*, **63**, 4926–4936, https://doi.org/10.1016/j.egypro.2014.11.523

Furre, A.-K., Meneguolo, R., Pinturier, L. and Bakke, K. 2020. Planning deep subsurface CO_2 storage monitoring for the Norwegian full-scale CCS project. *First Break*, **38**, 55–60, https://doi.org/10.3997/1365-2397.fb2020074

Fyfe, L.-J. and Underhill, J.R. 2023. The Upper Permian Zechstein Supergroup of NE England and the Adjacent Southern North Sea: a review of its role in the UK's energy transition. *Journal of Petroleum Geology*, **46**, 383–406, https://doi.org/10.1111/jpg.12843

Gebauer, A., Jahr, T. and Jentzsch, G. 2007. Recording and interpretation/analysis of tiltsignals with five ASKANIA borehole tiltmeters at the KTB. *Review of Scientific Instruments*, **78**, 054501, https://doi.org/10.1063/1.2736506

Geluk, M.C. and Röhling, H.-G. 1997. High-resolution sequence stratigraphy of the Lower Triassic 'Buntsandstein' in the Netherlands and northwestern Germany. *Geologie en Mijnbouw*, **76**, 227–246, https://doi.org/10.1023/A:1003062521373

Gibson-Poole, C.M., Taplin, M., Bouffin, N., Duffy, L., Sutherland, F., Cabral, A. and Ashby, D. 2024. Site characterization of the endurance CO_2 store, Southern North Sea, UK. *Geoenergy*, **2**, https://doi.org/10.1144/geoenergy2024-012

Glennie, K.W. 1990. Outline of North Sea history and structural framework. *In*: Glennie, K.W. (ed.) *Introduction to the Petroleum Geology of the North Sea*. Blackwell Scientific, Oxford, UK, 34–77.

Gluyas, J.G. and Bagudu, U. 2020. The endurance CO_2 storage site, blocks 42/25 and 43/21, UK North Sea. *Geological Society, London, Memoirs*, **50**, 163–171, https://doi.org/10.1144/m52-2019-47

Goertz-Allmann, B.P., Langet, N. *et al.* 2024. Effective microseismic monitoring of the Quest CCS site, Alberta, Canada. *International Journal of Greenhouse Gas Control*, **133**, https://doi.org/10.1016/j.ijggc.2024.104100

Grant, R.J., Underhill, J.R., Hernández-Casado, J., Jamieson, R.J. and Williams, R.M. 2019. The evolution of the dowsing graben system: implications for petroleum prospectivity in the UK Southern North Sea. *Petroleum Geoscience*, **27**, https://doi.org/10.1144/petgeo2018-064

Grant, R.J., Booth, M.G., Underhill, J.R. and Bell, A. 2020. Structural evolution of the Breagh area: implications for carboniferous prospectivity of the Mid North Sea High, Southern North Sea. *Petroleum Geoscience*, **26**, 174–203, https://doi.org/10.1144/petgeo2019-100

Griffiths, P.A., Allen, M.R., Craig, J., Fitches, W.R. and Whittington, R.J. 1995. Distinction between fault and salt control of Mesozoic sedimentation on the southern margin of the Mid-North Sea High. *Geological Society, London, Special Publications*, **91**, 145–159, https://doi.org/10.1144/GSL.SP.1995.091.01.08

Grude, S., Landrø, M. and Dvorkin, J. 2014. Pressure effects caused by CO_2 injection in the Tubåen Fm., the Snøhvit field. *International Journal of Greenhouse Gas Control*, **27**, 178–187, https://doi.org/10.1016/j.ijggc.2014.05.013

Hall, H.N. 1953. Compressibility of reservoir rocks. *Journal of Petroleum Technology*, **5**, 17–19, https://doi.org/10.2118/953309-G

Hammond, G.E. 2016. *PFLOTRAN: Practical Application of High-Performance Computing to Subsurface Simulation*. Technical Report SAND2016-5317C. Sandia National Laboratories (SNL-NM), Albuquerque, NM.

Hannis, S., Bricker, S., Goater, A., Holloway, S., Rushton, J., Williams, G. and Williams, J. 2013. Cross-international boundary effects of CO_2 injection. *Energy Procedia*, **37**, 4927–4936, https://doi.org/10.1016/j.egypro.2013.06.404

Hansen, O., Gilding, D. *et al.* 2013. Snøhvit: The history of injecting and storing 1 Mt CO_2 in the fluvial Tubåen Fm. *Energy Procedia*, **37**, 3565–3573, https://doi.org/10.1016/j.egypro.2013.06.249

Harrington, J.F., Birchall, D.J., Noy, D.J. and Cuss, R.J. 2007. *Consolidation and Mass Transport Properties of the Nordland Shale*. BGS Commissioned Report CR/07/210. British Geological Survey (BGS), Keyworth, Nottingham, UK, https://nora.nerc.ac.uk/id/eprint/17303

Harrington, J.F., Graham, C.C., Tamayo-Mas, E. and Parkes, D. 2018. Stress controls on transport properties of the Mercia Mudstone Group: Importance for hydrocarbon depletion and CO_2 injection. *Marine and Petroleum Geology*, **93**, 391–408, https://doi.org/10.1016/j.marpetgeo.2018.02.009

Hartmann, A. and Pechnig, R. 2008. Petrophysical analysis of regional-scale thermal properties for improved simulations of geothermal installations and basin-scale heat and fluid flow. *International Journal of Earth Sciences (Geologische Rundschau)*, **97**, 421–433, https://doi.org/10.1007/s00531-007-0283-y

Heinemann, N., Wilkinson, M., Pickup, G.E., Haszeldine, R.S. and Cutler, N.A. 2012. CO_2 storage in the offshore UK Bunter Sandstone Formation. *International Journal of Greenhouse Gas Control*, **6**, 210–219, https://doi.org/10.1016/j.ijggc.2011.11.002

Hillis, R.R. 2000. Pore pressure/stress coupling and its implications for seismicity. *Exploration Geophysics*, **31**, 448–454, https://doi.org/10.1071/EG00448

Hollinsworth, A.D., de Jonge-Anderson, I., Underhill, J.R. and Jamieson, R.J. 2022. Geological evaluation of suprasalt carbon storage opportunities in the Silverpit Basin, United Kingdom Southern North Sea. *AAPG Bulletin*, **106**, 1791–1825, https://doi.org/10.1306/03232221119

Hollinsworth, A.D., de Jonge-Anderson, I., Underhill, J.R. and Jamieson, R.J. 2024. Impact of reservoir quality on the carbon storage potential of the Bunter Sandstone Formation, Southern North Sea. *Geoenergy*, **2**, https://doi.org/10.1144/geoenergy2023-037

Horne, R.N. 1990. *Modern Well Test Analysis: A Computer-Aided Approach*. Petroway Inc., Palo Alto, CA.

Hossain, S., Hampson, G.J., Jacquemyn, C., Jackson, M.D. and Chiarella, D. 2024. Permeability characterisation of sedimentological facies in the Bunter Sandstone Formation, Endurance CO_2 storage site, offshore UK. *International Journal of Greenhouse Gas Control*, **135**, https://doi.org/10.1016/j.ijggc.2024.104140

IFC 2010. *International Formulation Committee of the Sixth International Conference on Properties of Steam*. International Association for the Properties of Water and Steam (IAPWS).

Jalalh, A.A. 2006*a*. Compressibility of porous rocks: part I. Measurements of Hungarian reservoir rock samples. *Acta Geophysica*, **54**, 319–332, https://doi.org/10.2478/s11600-006-0025-8

Jalalh, A.A. 2006*b*. Compressibility of porous rocks: part II. New relationships. *Acta Geophysica*, **54**, 399–412, https://doi.org/10.2478/s11600-006-0029-4

Jin, M., Pickup, G. and Mackay, E. 2010. *CASSEM Report of WP 2 (Rock Mechanics, Geochemistry and Reservoir Modelling). Simulation of Aquifer Storage of CO_2, Phase III*. Technical Report. Institute of Geoenergy Engineering, Heriot-Watt University, Edinburgh.

Johnson, H., Warrington, G. and Stoker, S.J. 1994. Permian and Triassic of the Southern North Sea. *In:* Knox, R.W.O'B. and Cordey, W.G. (eds) *Lithostratigraphic Nomenclature of the UK North Sea: Part 6*. British Geological Survey (BGS) on behalf of the UK Offshore Operators Association, Keyworth, Nottingham, UK, 1–141, https://webapps.bgs.ac.uk/data/Publications/publication.html?id=19867990

Kleiner, S. 2003. *Untersuchungen zur Optimierung von Erdwarmesondenanlagen – Petrophysikalische Messungen und numerische Simulationen*. Diploma thesis, RWTH Aachen University, Aachen, Germany, http://www.geophysik.rwth-aachen.de/html/diplomarbeiten.htm

McDermott, C., Williams, J. *et al.* 2016. Screening the geomechanical stability (thermal and mechanical) of shared multi-user CO_2 storage assets: A simple effective tool applied to the Captain Sandstone Aquifer. *International Journal of Greenhouse Gas Control*, **45**, 43–61, https://doi.org/10.1016/j.ijggc.2015.11.025

Morris, H.A., Williams, J.D.O., Abel, L.E., Hough, E., Field, L.P. and Parsons, R. 2026. Evaluation of the Röt Halite Member as a top seal for carbon dioxide storage in the Southern North Sea. *Geoenergy*, **4**, https://doi.org/10.1144/geoenergy2025-029

National Grid 2016*a*. *K43: Field Development Report*. Key Knowledge Document. Department of Energy and Climate Change, London, https://assets.publishing.service.gov.uk/government/uploads/system/uploads/attachment_data/file/531187/K43_Field_Development_Report.pdf

National Grid 2016*b*. *K40: Subsurface Geoscience and Production Chemistry Reports*. Key Knowledge Document. Department of Energy and Climate Change, London, https://assets.publishing.service.gov.uk/government/uploads/system/uploads/attachment_data/file/531045/K40_Subsurface_Geoscience_and_Production_Chemistry.pdf

Noy, D.J., Holloway, S., Chadwick, R.A., Williams, J.D.O., Hannis, S.A. and Lahann, R.W. 2012. Modelling large-scale carbon dioxide injection into the Bunter Sandstone in the UK Southern North Sea. *International Journal of Greenhouse Gas Control*, **9**, 220–233, https://doi.org/10.1016/j.ijggc.2012.03.011

Olden, P., Pickup, G., Jin, M., Mackay, E., Hamilton, S., Somerville, J. and Todd, A. 2012. Use of rock mechanics laboratory data in geomechanical modelling to increase confidence in CO_2 geological storage. *International Journal of Greenhouse Gas Control*, **11**, 304–315, https://doi.org/10.1016/j.ijggc.2012.09.011

Onuma, T. and Ohkawa, S. 2009. Detection of surface deformation related with CO_2 injection by DInSAR at In Salah, Algeria. *Energy Procedia*, **1**, 2177–2184, https://doi.org/10.1016/j.egypro.2009.01.283

OpenGoSim 2021. *The Mathematical Formulation of GAS_WATER*. OpenGoSim Ltd, Taunton, UK, https://docs.opengosim.com/cirrus/theory/mathematical_formulation_of_gw.html

Parkes, D., Busby, J., Kemp, S.J., Petitclerc, E. and Mounteney, I. 2021. The thermal properties of the Mercia Mudstone Group. *Quarterly Journal of Engineering Geology and Hydrogeology*, **54**, https://doi.org/10.1144/qjegh2020-098

Pevzner, R., Isaenkov, R. *et al.* 2021. Seismic monitoring of a small CO_2 injection using a multi-well DAS array: operations and initial results of Stage 3 of the CO2CRC Otway project. *International Journal of Greenhouse Gas Control*, **110**, https://doi.org/10.1016/j.ijggc.2021.103437

Pluymaekers, M.P.D., Doomenbal, J.C. and Middelburg, H. 2017. *Velmod-3.1*. TNO Report TNO 2017 R11014. TNO Geological Survey of the Netherlands, Utrecht, The Netherlands, https://www.nlog.nl/sites/default/files/2018-11/060.26839%20R11014%20with%20erratum%20page%2067%20Doornenbal-final.sec_.pdf

Raymond, J., Langevin, H., Comeau, F.-A. and Malo, M. 2022. Temperature dependence of rock salt thermal conductivity: Implications for geothermal exploration. *Renewable Energy*, **184**, 26–35, https://doi.org/10.1016/j.renene.2021.11.080

Ringrose, P.S., Furre, A.-K. *et al.* 2021. Storage of carbon dioxide in saline aquifers: Physiochemical processes, key constraints, and scale-up potential. *Annual Review of Chemical and Biomolecular Engineering*, **12**, 471–494, https://doi.org/10.1146/annurev-chembioeng-093020-091447

Robertson, E.C., Robie, R.A. and Books, K.G. 1958. *Physical Properties of Salt, Anhydrite and Gypsum*. United States Geological Survey Trace Elements Memorandum Report 1048, https://pubs.usgs.gov/tem/1048/report.pdf

Rushton, J.C., Hannis, S., Pearce, J., Williams, J. and Milodowski, A.E. 2025. Diagenetic evolution of the Bunter Sandstone Formation and its controls on reservoir quality: implications for CO_2 injectivity and storage. *Geoenergy*, **3**, https://doi.org/10.1144/geoenergy2024-023

Samperi, L., Giorgio, M. *et al.* 2020. Estimation of the physical, petrophysical and mineralogical properties of Messinian salt rocks, Sicily: Implications for multidisciplinary applications. *Marine and Petroleum Geology*, **112**, https://doi.org/10.1016/j.marpetgeo.2019.104032

Schlumberger 2017. VISAGE Technical Description, Version 2017.2, 90.

Shoulders, S. and Hodgkinson, J. 2024. A process-led approach to framing uncertainty and risk in CO_2 storage in the subsurface. *Geoenergy*, **2**, https://doi.org/10.1144/geoenergy2024-011

Skjaeveland, S.M., Siqveland, L.M., Kjosavik, A., Hammervold Thomas, W.L. and Virnovsky, G.A. 2000. Capillary pressure correlation for mixed-wet reservoirs. *SPE Reservoir Evaluation & Engineering*, **3**, 60–67, https://doi.org/10.2118/60900-PA

Smith, D.J., Noy, D.J., Holloway, S. and Chadwick, R.A. 2011. The impact of boundary conditions on CO_2 storage capacity estimation in aquifers. *Energy Procedia*, **4**, 4828–4834, https://doi.org/10.1016/j.egypro.2011.02.449

Spain, J.D. and Conrad, C.P. 1997. Quantitative analysis of top-seal capacity: offshore Netherlands, Southern North Sea. *Geologie en Mijnbouw*, **76**, 217–226, https://doi.org/10.1023/A:1003056609771

Span, R. and Wagner, W. 1996. A new equation of state for carbon dioxide covering the fluid region from the triple-point temperature to 1100 K at pressures up to 800 MPa. *Journal of Physical and Chemical Reference Data*, **25**, 1509–1596, https://doi.org/10.1063/1.555991

Stewart, S.A. and Coward, M.P. 1995. Synthesis of salt tectonics in the southern North Sea, UK. *Marine and Petroleum Geology*, **12**, 457–475, https://doi.org/10.1016/0264-8172(95)91502-G

Tsuji, T., Ikeda, T. *et al.* 2021. Continuous monitoring system for safe managements of CO_2 storage and geothermal reservoirs. *Scientific Reports*, **11**, 19120, https://doi.org/10.1038/s41598-021-97881-5

Underhill, J.R. 2003. The tectonic and stratigraphic framework of the United Kingdom's oil and gas fields. *Geological Society, London, Memoirs*, **20**, 17–59, https://doi.org/10.1144/GSL.MEM.2003.020.01.04

Underhill, J.R. 2009. Role of intrusion-induced salt mobility in controlling the formation of the enigmatic 'Silverpit Crater', UK Southern North Sea. *Petroleum Geoscience*, **15**, 197–216, https://doi.org/10.1144/1354-079309-843

Underhill, J.R., De Jonge-Anderson, I., Hollinsworth, A.D. and Fyfe, L.C. 2023. Use of exploration methods to repurpose and extend the life of a super basin as a carbon storage hub for the energy transition. *AAPG Bulletin*, **107**, 1419–1474, https://doi.org/10.1306/04042322097

Van Hoorn, B. 1987. Structural evolution, timing and tectonic style of the Sole Pit inversion. *Tectonophysics*, **137**, 239–284, https://doi.org/10.1016/0040-1951(87)90322-2

Vasco, D.W., Ferretti, A. and Novali, F. 2008. Reservoir monitoring and characterization using satellite geodetic data: interferometric synthetic aperture radar observations from the Krechba field, Algeria. *Geophysics*, **73**, WA113–WA122, https://doi.org/10.1190/1.2981184

Verdon, J.P., Kendall, J.-M., Stork, A.L., Chadwick, R.A., White, D.J. and Bissell, R.C. 2013. Comparison of geomechanical deformation induced by megatonne-scale CO_2 storage at Sleipner, Weyburn, and In Salah. *Proceedings of the National Academy of Sciences of the United States of America*, **110**, E2762–E2771, https://doi.org/10.1073/pnas.1302156110

Vosper, H., Chadwick, A., Williams, J., Newell, A., Vincent, C. and Quinn, M. 2017. The impact of deformation bands in fault zones on permeability: an upscaling approach. *In*: *Handling Fault Seals, Baffles, Barriers and Conduits*. Energy Group, Geological Society, London, 85–86, https://www.geolsoc.org.uk/science-and-policy/specialist-groups/energy-group/energy-group-resources/2017/

Weatherford Laboratories 2015. *NGC Laboratory Services for Special Core Analysis. National Grid Carbon Limited Humber Area – Bunter*. Weatherford UK Ltd, Dorchester, Dorset, UK, https://ndr.ogauthority.co.uk/

Wiese, B., Nimtz, M., Klatt, M. and Kühn, M. 2010. Sensitivities of injection rates for single well CO_2 injection into saline aquifers. *Chemie der Erde – Geochemistry*, **70**, 165–172, https://doi.org/10.1016/j.chemer.2010.05.009

Williams, J.D.O. 2025. Pore pressure data from the Bunter Sandstone Formation, Southern North Sea of the UK Continental Shelf. NERC Environmental Data Service (NERC EDS) National Geoscience Data Centre [Dataset], https://doi.org/10.5285/530ccd12-bfca-4112-b25c-e8c929f74964

Williams, J.D.O., Bentham, M., Jin, M., Pickup, G., Mackay, E., Gammer, D. and Green, A. 2013*a*. The effect of geological structure and heterogeneity on CO_2 storage in simple 4-way dip structures; a modelling study from the UK Southern North Sea. *Energy Procedia*, **37**, 3980–3988, https://doi.org/10.1016/j.egypro.2013.06.297

Williams, J.D.O., Jin, M., Bentham, M., Pickup, G.E., Hannis, S.D. and Mackay, E.J. 2013*b*. Modelling carbon dioxide storage within closed structures in the UK Bunter Sandstone Formation. *International Journal of Greenhouse Gas Control*, **18**, 38–50, https://doi.org/10.1016/j.ijggc.2013.06.015

Williams, J.D.O., Holloway, S. and Williams, G.A. 2014. Pressure constraints on the CO_2 storage capacity of the saline water-bearing parts of the Bunter Sandstone Formation in the UK Southern North Sea. *Petroleum Geoscience*, **20**, 155–167, https://doi.org/10.1144/petgeo2013-019

Williams, J.D.O., Fellgett, M.W., Kingdon, A. and Williamson, J.P. 2015. *In-situ* stress orientations in the UK Southern North Sea: Regional trends, deviations and detachment of the post-Zechstein stress field. *Marine and Petroleum Geology*, **67**, 769–784, https://doi.org/10.1016/j.marpetgeo.2015.06.008

Williams, J.D.O., Fellgett, M.W. and Quinn, M.F. 2016. Carbon dioxide storage in the Captain Sandstone aquifer: determination of *in situ* stresses and fault-stability analysis. *Petroleum Geoscience*, **22**, 211–222, https://doi.org/10.1144/petgeo2016-036

Zoback, M.D., Barton, C.A. *et al.* 2003. Determination of stress orientation and magnitude in deep wells. *International Journal of Rock Mechanics and Mining Sciences*, **40**, 1049–1076, https://doi.org/10.1016/j.ijrmms.2003.07.001

Zweigel, P. and Heill, L.K. 2003. *Studies on the Likelihood for Caprock Fracturing in the Sleipner CO_2 Injection Case – A Contribution to the Saline Aquifer CO_2 Storage (SACS) Project*. SINTEF Petroleum Research Technical Report 33.5324.00/02/03. SINTEF Petroleum Research, Trondheim, Norway, https://www.sintef.no/globalassets/project/ik23430000-sacs/technical-reports/zweigel_and_heill_caprock_fracturing_likelihood_report.pdf